ARTICLE IN PRESS

Nature Communications

https://doi.org/10.1038/s41467-026-71312-3

Article in Press

Thinner-than-paper and broad-temperature-adaptive zinc-iodine batteries enabled by nanophase separated deep-eutectic hydrogel electrolytes

Received: 23 July 2025

Accepted: 3 March 2026

Cite this article as: Shen, T., Chen, Z.-J., Yang, Y. *et al.* Thinner-than-paper and broad-temperature-adaptive zinc-iodine batteries enabled by nanophase separated deep-eutectic hydrogel electrolytes. *Nat Commun* (2026). https://doi.org/10.1038/s41467-026-71312-3

Tianyu Shen 沈天宇, Zong-Ju Chen 宗 , Yongxin Yang 永欣, Qianchuan Yu 余潜川, Jingyi Wang 王景毅, Kexin Hou 侯可心, Wei Meng 孟 , Junchuan Liang 梁俊川, Yiming Yang 一 , Hongguang Liu 刘洪广, Zuoxiu Tie 祚庥, Cheng-Hui Li 李承 & Zhong Jin 金

We are providing an unedited version of this manuscript to give early access to its findings. Before final publication, the manuscript will undergo further editing. Please note there may be errors present which affect the content, and all legal disclaimers apply.

If this paper is publishing under a Transparent Peer Review model then Peer Review reports will publish with the final article.

ARTICLE IN PRESS

© The Author(s) 2026. **Open Access** This article is licensed under a Creative Commons Attribution-NonCommercial-NoDerivatives 4.0 International License, which permits any non-commercial use, sharing, distribution and reproduction in any medium or format, as long as you give appropriate credit to the original author(s) and the source, provide a link to the Creative Commons licence, and indicate if you modified the licensed material. You do not have permission under this licence to share adapted material derived from this article or parts of it. The images or other third party material in this article are included in the article's Creative Commons licence, unless indicated otherwise in a credit line to the material. If material is not included in the article's Creative Commons licence and your intended use is not permitted by statutory regulation or exceeds the permitted use, you will need to obtain permission directly from the copyright holder. To view a copy of this licence, visit http://creativecommons.org/licenses/by-nc-nd/4.0/.

ARTICLE IN PRESS

TITLE

Thinner-Than-Paper and Broad-Temperature-Adaptive Znic-Iodine Batteries Enabled by Nanophase Separated Deep-Eutectic Hydrogel Electrolytes

AUTHOR LIST

Tianyu Shen (沈天宇)[#,1,2,3,4], Zong-Ju Chen (陈宗举)[#,1], Yongxin Yang (杨永欣)[1,3,4], Qianchuan Yu (余潜川)[1,3,4], Jingyi Wang (王景毅)[1,3,4], Kexin Hou (侯可心)[1], Wei Meng (孟伟)[1], Junchuan Liang (梁俊川)[1,3,4], Yiming Yang (杨一鸣)[1,3,4], Hongguang Liu (刘洪广)[1,3,4], Zuoxiu Tie (铁祚庥)[1,3,4], Cheng-Hui Li (李承辉)[*,1], and Zhong Jin (金钟)[*,1,2,3,4]

AFFILIATIONS

[1] State Key Laboratory of Coordination Chemistry, MOE Key Laboratory of Mesoscopic Chemistry, MOE Key Laboratory of High Performance Polymer Materials and Technology, School of Chemistry and Chemical Engineering, Nanjing University, Nanjing, Jiangsu 210023, P. R. China.

[2] School of Chemistry and Chemical Engineering, Suzhou University, Suzhou, Anhui 234000, P. R. China.

[3] Jiangsu Key Laboratory of Green Energy Catalysis and Intelligent Chemical Engineering, Suzhou Key Laboratory of Green Intelligent Manufacturing of New Energy Materials and Devices, Institute of Green Chemistry and Engineering, Nanjing University, Suzhou, Jiangsu 215163, P. R. China.

[4] Tianchang New Materials and Energy Technology Research Center of Nanjing University, Tianchang, Anhui 239300, P. R. China.

[#] These authors contributed equally: Tianyu Shen, Zong-Ju Chen.

[*]E-mail address of corresponding authors: chli@nju.edu.cn (C. H. Li), zhongjin@nju.edu.cn (Z. Jin)

ARTICLE IN PRESS

ARTICLE IN PRESS

ABSTRACT

Hydrogel electrolyte based secondary batteries are promising for wearable electronics, yet face challenges including limited mechanical resilience, and narrow temperature range. Herein, we report a robust deep-eutectic hydrogel electrolyte fabricated via synergistic interplay of dual nanophase separation, hydrated eutectic solvation, and hydrogen-bond networks. The interwoven nanophase separation architecture, integrating hydrophilic polyvinyl alcohol phases and hydrophobic polyacrylonitrile phases, realizes high fracture-strength (4.1 MPa) and toughness (13.66 MJ m^{-3}). Meanwhile, deep-eutectic chemistry modulates Zn^{2+} solvation structures and leverages cyano-coordination channels of polyacrylonitrile to achieve high Zn^{2+} ionic conductivity (28.2 mS cm^{-1}) and transference number (0.65) at 20 °C. Concurrently, abundant hydrogen bonds induced by multiple donor sites of hydrophilic phases, urethane, and $Zn(ClO_4)_2$ immobilize active H_2O to ensure broad-temperature durability. This tripartite synergy directs planar Zn deposition along (002) planes and suppresses dendrite growth, enabling Zn||I_2 batteries with a thinner-than-paper thickness (42 μm) and high flexibility. The assembled Zn||I_2 batteries demonstrate high specific energy (108.99 Wh kg^{-1}) and cycling stability (over 36,000 cycles under −40 to 80 °C). In this work, the convergence of molecule design, phase modulation, and process engineering establishes a feasible methodological framework for developing advanced flexible batteries that integrate high energy density and harsh environment tolerance.

INTRODUCTION

Aqueous zinc-metal batteries have emerged as promising candidates for next-generation energy storage, owing to their inherent safety, cost-effectiveness, and environmental compatibility.[1-9] However, conventional liquid electrolytes (LE) suffer from critical limitations, including leakage susceptibility, narrow temperature range, and uncontrolled zinc dendrite growth, which severely restrict their practical deployment.[10-14] Hydrogel electrolytes (HE), particularly polyvinyl alcohol (PVA)-derived HEs, can somewhat lock up water molecules by hydrogen bonds and inhibit dendrite growth, but still remain plagued by intrinsic trade-offs.[15-21] Specifically, HE systems

ARTICLE IN PRESS

often restricted by the reconcile mechanical robustness with electrochemical performance, the excessive free water content that compromises temperature adaptability, and the thickness usually exceeding 100 μm that diminish energy density.[22-29] Although phase-separated HE, as demonstrated in our prior work, have shown enhanced modulus and dendrite suppression, it remains a significant challenge to achieve simultaneous advances in thin geometries, broad-temperature resilience, and electrochemical stability.[30]

Herein, we present the fabrication of a robust deep-eutectic HE (deep-eutectic-HE) via synergistic integration of nanophase separation, hydrated eutectic solvation, and hydrogen-bond networks. The interwoven nanophase separation architecture, engineered through solvent-exchange, establishes a dual-domain structure comprising hydrophilic PVA phases and hydrophobic polyacrylonitrile (PAN) phases, endowing the hydrogel with good mechanical properties (4.1 MPa fracture strength and 13.66 MJ m^{-3} toughness). Concurrently, hydrogen-bond interactions between hydrophilic phases, urethane (UR) moieties, water molecules, and ClO_4^- ions immobilize active water, enabling stable operation across a broad temperature range (−40 to 80 °C). Deep-eutectic chemistry and cyano-coordination pathways of PAN collaboratively reconfigure Zn^{2+} solvation structures, achieving high ionic conductivity (28.2 mS cm^{-1}) and Zn^{2+} transference numbers (0.65), while suppressing polyiodide shuttling. This tripartite synergy directs planar Zn deposition on (002) crystallographic planes and mitigates dendrite formation, enabling Zn||I_2 full batteries with a thinner-than-paper thickness (42 μm) and high flexibility that deliver stable power under mechanical deformation (180° bending). The as-assembled Zn||I_2 pouch battery achieves high specific energy and volumetric energy density (108.99 Wh kg^{-1} and 189.41 Wh L^{-1}), rate capability, and long lifespan under broad temperatures (with 92.31%, 75.28%, and 81.00% capacity retention after 36,000 cycles at −40, 20, and 80 °C, respectively). By synergistically optimizing molecular compositions, phase structures, and fabrication processes, a practical systematic approach is built to engineer advanced flexible batteries that simultaneously achieve good energy storage capacity and resistance to harsh environments.

ARTICLE IN PRESS

RESULTS

Design, preparation, and characterizations of deep-eutectic-HE

In this work, we propose a synergistic architectural strategy to construct a robust deep-eutectic-HE capable of reconciling thin geometries with good mechanical properties, electrochemical performances, and temperature adaptability. The stepwise fabrication strategy is realized by integrated manipulation of nanophase separation, hydrated eutectic solvation, and hydrogen-bond networks in the HE matrix, as presented in Fig. 1a. Typically, the fabrication paradigm commences with dimethyl sulfoxide (DMSO) mediated dissolution of polyvinyl alcohol (PVA) and acrylonitrile (AN). The strong hydrogen-bond disrupting capability of DMSO enables nearly complete dissociation of intra- and inter-chain interactions, yielding a homogeneous polymeric precursor.[31] Subsequent heating initiates the polymerization of AN, driving the in-situ formation of a dual-network PAN-PVA composite through progressive crosslinking and chain entanglement. Finally, the DMSO removal and Zn^{2+} electrolyte exchange step establishes uniform polymer-electrolyte integration, and also optimizes zinc ion solvation structure via competitive coordination between unsaturated cyano groups and water molecules.[30] During this phase evolution process, hydrophilic phases (rooted in the hydrophilic hydroxyl groups on PVA chains) and hydrophobic phases (formed via dipole-dipole interactions of PAN segments) spontaneously organize into a dual-nanophase separated architecture. This architecture, in synergy with the crystalline domains formed by a part of PVA segments, significantly enhances the mechanical strength of deep-eutectic-HE. Simultaneously, the hydrophilic hydroxyl groups of PVA contribute to expanding the polymer network, increasing the content of hydrated eutectic solvent in the hydrogel and forming abundant hydrogen bonds with H_2O to reduce the activity of H_2O. Moreover, the hydrophobic cyano groups on PAN chains construct a rapid transfer channel for Zn^{2+}, thereby improving the electrochemical kinetics of deep-eutectic-HE.[30, 32]

To benchmark the advantages of deep-eutectic-HE across mechanical and electrochemical properties, we chose the non-gelated deep-eutectic liquid electrolytes ($H_2O/Zn(ClO_4)_2$/UR, namely deep-eutectic-LE), the non-eutectic liquid electrolytes ($H_2O/Zn(ClO_4)_2$, namely non-eutectic-LE),

ARTICLE IN PRESS

and gelated non-eutectic-LE (namely non-eutectic-HE) as the control groups. The attenuated total reflection Fourier transform infrared (ATR-FTIR) spectra (Fig. 1b) revealed critical molecular interactions among UR, $Zn(ClO_4)_2$, and trace H_2O. Compared with non-eutectic-HE and non-eutectic-LE, the N–H asymmetric stretching vibrations (3325 and 3415 cm^{-1}) of deep-eutectic-HE and deep-eutectic-LE underwent a 54–66 cm^{-1} blue shift accompanied by peak broadening upon eutectic formation, indicating hydrogen-bond reorganization between UR molecules, water clusters, and ClO_4^- anions due to the addition of UR. Simultaneously, the C=O stretching vibration of deep-eutectic-HE and deep-eutectic-LE red-shifted by 6 cm^{-1} (1687 → 1681 cm^{-1}), confirming Zn^{2+} coordination to carbonyl oxygen atoms within UR.[32] Complementary Raman analyses (Fig. 1c) demonstrated vibrational mode modifications consistent with this interaction. The C–N and N–H stretching frequencies of UR in deep-eutectic-HE and deep-eutectic-LE shifted by +17 and +10 cm^{-1} respectively, reinforcing evidence for three-dimensional hydrogen-bond network formation.[32]

Scanning electron microscopy (SEM) image of deep-eutectic-HE (Fig. 1d) revealed a well-defined nanophase-separated structure with phase dimensions of 10–30 nm, substantially below the wavelengths of visible light (400–700 nm). This contrasts sharply with non-eutectic-HE (Supplementary Fig. 1), where the salting-in effect induced by excess ions suppresses phase separation, resulting in a porous morphology with limited hierarchical structure.[33] Specifically, the poorly hydrated chaotropes anions (ClO_4^-) will induce hydrophilic effects of the polymer chain segments, while weakening the hydrogen bonds between polymer chain segments, causing the polymer to dissolve (i.e., salting in). Consequently, the compaction degree of the PVA network is significantly reduced, making it difficult to form a nanoscale phase separation structure with PAN.[34] The atomic force microscopy (AFM) mapping (Fig. 1e and Supplementary Fig. 2-3) further validated the nanophase-separated structure of deep-eutectic-HE, revealing its phase size of 20 nm approximately.[33] The small-scale nanophase separation structure not only significantly enhanced the toughness of deep-eutectic-HE, but also improved its transparency. The optical implications of this nano-structuring become apparent in Supplementary Fig. 4, where both deep-

ARTICLE IN PRESS

eutectic-HE and non-eutectic-HE exhibit >90% visible-light transmittance – a direct consequence of subwavelength phase-separation dimensions.[30] X-ray diffraction (XRD) patterns (Fig. 1f) provided crystallographic evidence for enhanced structural order, with deep-eutectic-HE displaying intensified (101) and (200) diffraction peaks of PVA at 18.0° and 21.3°, respectively. This improved crystallinity established a structural foundation for good mechanical performance through optimized polymer chain packing.[35] Given the complexity of structural domains of deep-eutectic-HE, small-angle X-ray scattering (SAXS) profiles (Fig. 1g) further quantitatively resolved the nanophase-separated structure, revealing two characteristic distances at 25.7 nm and 10.9 nm corresponding to hydrophobic and crystalline domain spacing, respectively.[36] These dimensions, which aligned with SEM-observed phase separation, also explained the enhanced optical clarity and mechanical robustness of deep-eutectic-HE through nanoconfined polymer dynamics.

Mechanical Properties and Temperature Tolerance of deep-eutectic-HE

The mechanical properties of deep-eutectic-HE were systematically evaluated to elucidate the synergistic effects of nanophase-separated architecture, hydrated eutectic solvation, and hydrogen-bond network optimization. Tensile testing (Fig. 2a-b) demonstrated good mechanical properties in deep-eutectic-HE relative to non-eutectic-HE, with enhancements in fracture strain (752%), fracture strength (4.09 MPa), elastic modulus (1.84 MPa), and toughness (13.66 MJ m^{-3}). These good mechanical properties of deep-eutectic-HE stem from two complementary mechanisms. First, ClO_4^-, as chaotropic ions positioned on the right side of the Hofmeister series, typically induce polymer dissolution through salting-in effects.[37-38] In deep-eutectic-HE, however, UR-mediated hydrogen bonds with ClO_4^- mitigates this destabilizing interaction while reinforcing the hydrogel network. Second, replacing DMSO (a good solvent) with deep-eutectic-LE (a poor solvent) in deep-eutectic-HE shifts thermodynamic equilibria toward polymer chain association, promoting crystalline domain formation as evidenced by XRD analysis (Fig. 1f).[39] This nanophase separation engineering strategy enabled fabrication of thin deep-eutectic-HE membranes down to 6 μm thickness (Fig. 2c), which maintain strong load-bearing capacity by sustaining 2.2 kg weights

ARTICLE IN PRESS

without fracture (Fig. 2d) – a 44-fold improvement over non-eutectic-HE.

Differential scanning calorimetry (DSC) profiles in Fig. 2e also revealed distinct phase-transition behaviors among the four electrolyte samples. Deep-eutectic-HE and non-eutectic-HE demonstrated glass transition temperatures of −85.7 °C and −80.5 °C, whereas deep-eutectic-LE and non-eutectic-LE exhibited exothermic crystallization peaks at −43 and −81.8 °C, respectively. Benefiting from the high concentration of $Zn(ClO_4)_2$, non-eutectic-LE and non-eutectic-HE exhibit similar low freezing points.[40] For deep-eutectic-LE, the addition of UR increases hydrogen bonds with H_2O, restricting movements such as vibration or rotation of the H_2O molecules, resulting in an elevation in the glass transition temperature.[41] For deep-eutectic-HE, the dense network structure effectively confines H_2O molecules within nanoscale pores, thereby inhibiting the nucleation and growth of ice crystals.[42] Compared to non-eutectic-HE, the additional 5.2 °C glass transition temperature reduction in deep-eutectic-HE underscored the critical role of eutectic chemistry in optimizing low-temperature adaptability.

Thermal endurance characterization via DSC (Fig. 2f) also highlighted contrasting high-temperature responses. Neither deep-eutectic-HE nor deep-eutectic-LE displayed endothermic transitions between 20–120 °C, confirming their structural integrity under relatively high temperatures.[43] This stability arises from the capacity of deep-eutectic system to minimize free water content through UR-mediated hydrogen-bond networks and nanoconfined water states. In contrast, non-eutectic-HE and non-eutectic-LE underwent a phase transition at 72.3 and 74.0 °C due to unbound water evaporation, as evidenced by its larger number of hydrogen bonds among H_2O. Rheological profiling (Fig. 2g) corroborated this thermal endurance, showing stable storage modulus (G′) and loss modulus(G″) for deep-eutectic-HE during heating cycles versus progressive stiffening in non-eutectic-HE due to free water evaporation. Water retention studies (Supplementary Fig. 5) quantified the hydration dynamics underpinning this thermal stability: deep-eutectic-HE retained 88.4% water content after 48 h at 25 °C/15% RH, higher than non-eutectic-HE (78.5%) through UR-mediated water immobilization.

Molecular dynamics (MD) simulations (Fig. 2h and Supplementary Fig. 6) quantitatively resolved

ARTICLE IN PRESS

water confinement states in these electrolyte systems. Fig. 2j demonstrated that non-eutectic-HE and non-eutectic-LE contain the most hydration bonds between H_2O molecules, rendering them susceptible to both ice crystallization at low temperatures and dehydration-induced structural collapse at elevated temperatures. Conversely, deep-eutectic-HE and deep-eutectic-LE exhibited reduced number of hydrogen bonds, confirming effective water activity suppression through the combined effects of hydrogen-bond networks and eutectic solvent interactions. Moreover, deep-eutectic-HE exhibited an even lower number of hydrogen bonds compared to deep-eutectic-LE, attributed to the hydrogen-bond adsorption of H_2O by the polymer network of hydrophilic PVA phases. These MD results aligned well with DSC-observed thermal behaviors, indicating the restricted water mobility directly correlates with enhanced cryogenic performance and evaporation resistance.

MD simulation simultaneously unveiled alterations of Zn^{2+} solvation structures (Fig. 2i and Supplementary Fig. 6, with source data provided as Supplementary Data 1-8). For non-eutectic-LE, radial distribution function (RDF, g(r)) analysis confirmed a first solvation shell coordination number of 6 for H_2O around Zn^{2+} (Fig. 2k). Post-gelation, the emergence of coordination interactions between Zn^{2+} and cyano in PAN chains led to their incorporation into the first solvation shell, thereby diminishing the hydration number to 5.37. Strikingly, the introduction of UR induced a pronounced reduction in the hydration number within the first solvation shell of Zn^{2+}, dropping below 3 in both deep-eutectic-HE and deep-eutectic-LE systems. This substantial perturbation of the Zn^{2+} solvation structure correlated with an enhancement in the diffusion coefficient of Zn^{2+}, exhibiting a 9-fold increase in deep-eutectic-HE relative to the non-eutectic LE (Fig. 2l), thereby enabling its higher ionic conductivity.

Electrochemical performances of deep-eutectic-HE

The electrochemical performances of deep-eutectic-HE were systematically investigated through Zn||Zn and SS (stainless steel)||SS symmetric batteries. Temperature-dependent ionic conductivity profiling (Supplementary Fig. 7 and Table 1) demonstrated efficient charge transport capabilities

ARTICLE IN PRESS

of deep-eutectic-HE across −40 to 80 °C. The deep-eutectic-HE maintained 28.2 mS cm^{-1} ionic conductivity at 20 °C and retained 1.7 mS cm^{-1} at −40 °C. This is a direct consequence of hydrogen-bond-mediated water confinement that suppresses ice nucleation while preserving ion mobility. Comparative analyses (Fig. 3a, Supplementary Fig. 8 and Table 2-4) showed deep-eutectic-LE, non-eutectic-HE and non-eutectic-LE exhibited inferior room-temperature conductivities (11.0, 8.0, and 6.2 mS cm^{-1}, respectively), with deep-eutectic-LE becoming non-conductive below −40 °C due to crystalline phase formation. The structure of non-eutectic-HE collapsed at 80 °C (Supplementary Fig. 8c), further highlighting the critical role of UR-enhanced hydrogen-bond networks in stabilizing hydrated eutectic architectures.

Zn^{2+} transference number (t_{Zn}^{2+}) analyses (Fig. 3b and Supplementary Fig. 9) quantified Zn^{2+} transport kinetics of deep-eutectic-HE (t_{Zn}^{2+} = 0.62–0.68 across −40 to 80 °C), higher than deep-eutectic-LE (t_{Zn}^{2+} = 0.36–0.38), non-eutectic-HE (t_{Zn}^{2+} = 0.43–0.46) and non-eutectic-LE (t_{Zn}^{2+} = 0.41–0.46). This enhancement arises from synergistic effects: cyano groups on PAN chains coordinate with Zn^{2+} ions to establish rapid ionic migration channels while hydrogen-bond UR-ClO_4^- complexes restrict anion mobility, collectively restructuring the Zn^{2+} solvation structure (Fig. 2i).[44-47] Electrochemical impedance spectroscopy (EIS) measurements (Fig. 3c and Supplementary Table 5) revealed interfacial resistance values of 238.22 Ω for Zn|deep-eutectic-HE|Zn battery, significantly lower than those of deep-eutectic-LE (465.98 Ω), non-eutectic-HE (663.73 Ω) and non-eutectic-LE (599.18 Ω) counterparts, attributable to optimized electrode-electrolyte adhesion.

Rate performance evaluations (Fig. 3d and Supplementary Fig. 10) revealed that deep-eutectic-HE maintains a voltage polarization below 200 mV across a broad current density range (0.2–5.0 mA cm^{-2}), contrasting sharply with non-eutectic-HE, which exhibited large polarization (>5.0 V) at 5.0 mA cm^{-2}. This improved electrochemical performance of deep-eutectic-HE primarily stems from its optimized Zn^{2+} ion transport kinetics and reduced interfacial impedance.[48] Tafel analyses (Fig. 3e) corroborated these findings, showing its low corrosion current (0.06 μA cm^{-2}) and suppressed polarization behavior, again verifying its ability to achieve stable Zn^{2+} ion

ARTICLE IN PRESS

plating/stripping behavior.

Long-term cycling testing (Fig. 3f) demonstrated the improved electrochemical stability of deep-eutectic-HE, sustaining operation for 4200 h with minimal polarization (<100 mV at 0.5 mA cm^{-2} and 0.5 mAh cm^{-2}). This starkly contrasts with the rapid failures in deep-eutectic-LE (100 h), non-eutectic-HE (200 h), and non-eutectic-LE (230 h) where Zn dendrite penetration caused the short circuits of batteries. The Zn|deep-eutectic-HE|Zn symmetric battery exhibited highly reversible Zn plating/stripping behavior, unequivocally validating the synergistic advantages of deep-eutectic-HE: rapid Zn^{2+} ion transport kinetics, robust dendrite suppression capability, and prolonged cyclability.

Broad-temperature evaluations (Fig. 3g-3h) validated the broad temperature adaptability of deep-eutectic-HE. The critical working temperature tests of Zn||Zn symmetric batteries assembled with different electrolytes revealed that the Zn|deep-eutectic-HE|Zn symmetric battery could maintain stable electrochemical performance up to ~80 °C, which is better than those of deep-eutectic-LE (~70 °C), non-eutectic-HE (~50 °C), and non-eutectic-LE (~60 °C) counterparts (Supplementary Fig. 11). When the operation temperature was raised higher than the critical working temperature, significant ionic insulation would occur due to the precipitation of salts from solvent evaporation for LE samples or the collapse of gel structure for HE samples. The Zn|deep-eutectic-HE|Zn symmetric battery maintained stable cycling for more than 800 h with polarizations of 153.4 mV (at −40 °C) and 56.6 mV (at 80 °C), enabled by UR-H_2O hydrogen bonds that suppress H_2O-H_2O network formation. In contrast, non-eutectic-HE exhibited large voltage polarization (>1.0 V) at −40 °C, and failed at 80 °C due to structural collapse. Meanwhile, deep-eutectic-LE and non-eutectic-LE suffered rapid short-circuiting under high temperatures. In conclusion, deep-eutectic-HE displayed the ability to optimize ion transport kinetics, inhibit Zn dendrite growth, and maintain structural stability under demanding conditions.

The electrochemical stability window of deep-eutectic-HE was also investigated via linear sweep voltammetry. Supplementary Fig. 12 demonstrated that deep-eutectic-HE achieved an expanded electrochemical stability window (2.69 V), surpassing deep-eutectic-LE (2.57 V), non-eutectic-

ARTICLE IN PRESS

HE (2.49 V), and non-eutectic-LE (2.44 V). This enhancement arises from restricted water molecule mobility within the hydrogen-bond eutectic network, which suppresses parasitic reactions at elevated potentials. To contextualize these results, Fig. 3i and Supplementary Table 6-7 compared deep-eutectic-HE against other recent reported HEs across several critical performance parameters: fracture strength (4.09 MPa), ionic conductivity (28.2 mS cm^{-1}), electrochemical stability window (2.69 V), low-temperature tolerance (−40 °C), high-temperature tolerance (80 °C), film thickness (6 μm), coordination number of Zn-H_2O (2.71), Zn^{2+} transference number (0.65), cycling stability, and battery lifespan.[16, 30, 49-59] Overall, the as-proposed deep-eutectic-HE combines these attributes, establishing it as a multifunctional electrolyte platform.

Zinc electro-plating/stripping behaviors guided by deep-eutectic-HE

To comprehensively investigate the capacity of deep-eutectic-HE to regulate zinc deposition behavior, multi-scale analyses of Zn||Cu half batteries were conducted. Due to the inferior electrochemical performances of non-eutectic-HE and non-eutectic-LE, deep-eutectic-LE was chosen as a control group for subsequent tests. The average Coulombic efficiency, a critical metric for evaluating zinc utilization reversibility, was measured over 20 electro-plating/stripping cycles using the Aurbach method (Fig. 4a).[60] The deep-eutectic-HE achieved an average Coulombic efficiency of 98.47%, higher than deep-eutectic-LE (96.99%) by 1.48%. Voltage-time profiles (Fig. 4b) further revealed the reduced polarization of deep-eutectic-HE, with a 33% reduction in hysteresis compared to deep-eutectic-LE during the initial deposition phase.

Detailed overpotential analyses (Fig. 4c and Supplementary Fig. 13) quantified the kinetic advantages of deep-eutectic-HE. The nucleation overpotential (42.6 mV vs. 66.5 mV) and mass-transfer overpotential (22.0 mV vs. 46.4 mV) of deep-eutectic-HE relative to deep-eutectic-LE were reduced by 35.9% and 52.6%, respectively. These improvements stem from synergistic effects between molecular-scale coordination chemistry and macro-scale mechanical properties. At the atomic level, cyano groups along the polymer backbone in PAN form transient coordination complexes with Zn^{2+}, creating low-energy migration pathways that lower activation barriers for

ARTICLE IN PRESS

Zn^{2+} transport.[30] Macroscopically, the high elastic modulus of deep-eutectic-HE generates substantial mechanical resistance against the growth of zinc dendrites during zinc deposition, physically constraining vertical growth while promoting lateral spreading of Zn across the electrode surface.[30, 61, 62]

Cyclic voltammetry (CV) provided additional evidences on optimized reaction kinetics (Fig. 4d). The deep-eutectic-HE exhibited a peak response current density of 15.9 mA cm^{-2} with minimal polarization (33 mV) compared to deep-eutectic-LE (9.2 mA cm^{-2} and 68 mV). The 72.8% current density enhancement directly results from the coordinated action of accelerated Zn^{2+} mobility and spatially confined deposition geometry. This dual mechanism ensures rapid ion replenishment at the electrode-electrolyte interface while maintaining planar deposition morphology through stress distribution.

Crystallographic orientation analyses via XRD revealed fundamental differences in zinc deposition patterns (Fig. 4e). After 50 cycles (100 h), deep-eutectic-HE enhanced the (002) plane diffraction intensity by 40.97% relative to pristine zinc foil, indicating preferential horizontal growth along this low-surface-energy crystallographic orientation.[63-65] In sharp contrast, deep-eutectic-LE increased (101) plane dominance, promoting vertically zinc dendrite formation, ultimately leading to severe Zn dendrite growth. SEM analyses of cycled zinc negative electrodes in deep-eutectic-HE and deep-eutectic-LE revealed stark morphological contrasts. Fig. 4f demonstrates that deep-eutectic-HE enables horizontally aligned, layered zinc deposition, maintaining negative electrode surface uniformity over prolonged cycling. This planar growth mode ensures stable ion flux and interfacial integrity. In contrast, deep-eutectic-LE promotes vertical dendrite formation within 50 cycles, with progressive sharpening leading to severe surface roughness (Fig. 4g). After 200 cycles in deep-eutectic-LE, interconnected protrusions were observed on the Zn electrode, heightening the risks of separator penetration. XRD data (Fig. 4e) corroborate these findings, showing preferential horizontal (002) plane deposition in deep-eutectic-HE versus longitudinal crystallographic growth in deep-eutectic-LE. The zinc deposition behavior in different electrolytes was observed by in-situ optical microscopy (Supplementary Fig.

ARTICLE IN PRESS

14). In deep-eutectic-HE, the Zn surface is flat and smooth, without obvious protrusions throughout the whole deposition process. In contrast, in deep-eutectic-LE, Zn protrusions emerge on Zn surface after consecutive deposition for 20 min, and obvious Zn dendrites are observed after 40 min. These results are consistent well with the SEM observations (Fig. 4f-g), indicating that the deep-eutectic-HE is effective in inhibiting the growth of Zn dendrites. The combined XRD, SEM and in-situ optical microscopy evidences conclusively established the dual functionality of deep-eutectic-HE in sustaining electrochemical stability and enforcing dendrite-suppressive deposition, critical for long-term battery reliability.

Electrochemical performances of zinc-metal batteries

For practical validation, we constructed full batteries using zinc foil negative electrodes and iodine positive electrodes. To ensure compatibility with the thin deep-eutectic-HE (6 μm), I_2/carbon nanotubes (CNTs) composite positive electrode was developed by a convenient filtration and adsorption method (Supplementary Fig. 15). Zn||I_2 full batteries were then assembled with thin I_2/CNTs positive electrode (20 μm thick). The robust nanoarchitecture enables fabrication of 6-μm-thick deep-eutectic-HE membranes while resisting dendrite penetration (Supplementary Fig. 16-17). By integrating Zn foil negative electrode (10 μm), deep-eutectic-HE (6 μm), I_2/CNTs positive electrode (20 μm), and polyimide (PI) package (3 μm × 2), the Zn||I_2 full battery achieved high compactness (42 μm total thickness, Fig. 5a, g), representing 55% reduction compared to standard A4 paper (104 μm, ISO 216). The achieved thickness is competitive compared to some recent relevant reports.[16, 30, 49-56]

During the discharging process of Zn||I_2 batteries, I_2 in the positive electrode undergoes a reduction reaction and converts into I^-, which combines with Zn^{2+} in the electrolyte to form ZnI_2 and adsorbs in the positive electrode. Oppositely, a reverse pathway occurs during the charge process. Notably, the tailored eutectic chemical environment induces a paradigm shift in iodide ion chemistry through multi-scale confinement effects (Fig. 5a). The I^- solubility undergoes a three-order-of-magnitude reduction from 9.22 M in conventional aqueous systems to merely 0.79 M in deep-

ARTICLE IN PRESS

eutectic-LE (Supplementary Fig. 18), fundamentally inhibiting the loss of active substances and altering the iodine redox equilibrium ($I_2 + I^- \rightleftharpoons I_3^-$).[66] This dramatic solubility suppression originates from synergistic steric hindrance and electronic modulation. The hydrogen-bond network between UR, H_2O and ClO_4^- creates molecular-scale barriers that physically restrict I^- accommodation.[66] Density functional theory (DFT) simulations quantitatively verified this dual confinement mechanism. As illustrated in Supplementary Fig. 19a (with source data provided as Supplementary Data 9-12), the diffusion energy barrier for I^- migration increases exponentially from 1.98 eV in non-eutectic system to 3.69 eV in the deep-eutectic system. This is an 86% enhancement that effectively mitigates I_2 shuttling at the molecular level. Concurrently, the formation energy of I_3^- complexes rises by 32% (0.280 eV in deep-eutectic system vs. 0.173 eV in non-eutectic system, Supplementary Fig. 19b), indicating thermodynamic disfavoring of polyiodide generation. Moreover, the coordinated evolution of deep-eutectic-HE simultaneously locks activity water molecules via hydrogen bonds with UR and ClO_4^- ions while reducing Zn^{2+} hydration number, collectively conferring resistance to both low and high temperatures without sacrificing ionic transport efficiency.[43]

Rate capability tests in Fig. 5b revealed that the Zn|deep-eutectic-HE|I_2 battery maintains a specific discharge capacity of 198.39 mAh g^{-1} when returning to 0.5 A g^{-1} after high-rate cycling at 10 A g^{-1}, demonstrating 99.80% capacity retention relative to initial low-rate value. This improved reversibility contrasts sharply with the deep-eutectic-LE system, which exhibits rapid capacity degradation, delivering only 97.86 mAh g^{-1} at 10 A g^{-1} with 79.25% capacity recovery upon rate reduction (Fig. 5b and Supplementary Fig. 20). The enhanced rate performance of deep-eutectic-HE benefits from its faster Zn^{2+} transfer kinetics and higher zinc electro-deposition/stripping homogeneity.[20, 67-68] In contrast, the inferior rate performance of deep-eutectic-LE control sample originates from three synergistic limitations. Firstly, sluggish Zn^{2+} transport kinetics of deep-eutectic-LE arise from the unoptimized Zn^{2+} solvation structure, causing insufficient dissociation and reduced ionic conductivity under rapid ion flux demands at high rates. Secondly, the absence of a robust hydrogen-bond network in deep-eutectic-LE induces elevated interfacial impedance

ARTICLE IN PRESS

and uncontrolled Zn dendrite, both of which consuming active Zn and electrolyte, resulting in irreversible capacity loss. Thirdly, the low Zn^{2+} transference number of deep-eutectic-LE exacerbates a concentration polarization across electrodes at high rates, further limiting positive electrode capacity utilization. These factors collectively result in the poor rate performance of deep-eutectic-LE control sample.

Long-term cycling stability of Zn|deep-eutectic-HE|I_2 battery was assessed subsequently (Fig. 5c), maintaining a Coulombic efficiency of >99.5% over 36,000 cycles at 5 A g^{-1}, an initial specific capacity of 146.15 mAh g^{-1}, and a capacity retention of 75.28% (average decay: 0.0007% per cycle). When cycled at 2 A g^{-1}, the Zn|deep-eutectic-HE|I_2 battery also displayed an initial specific capacity of 170.28 mAh g^{-1} and a capacity retention of 65.77% (average decay: 0.0034% per cycle) after 10,000 cycles (Supplementary Fig. 21). Thermogravimetric analysis offered a clear explanation for the capacity degradation during long-term cycling (Supplementary Fig. 22).[59] After 10,000 cycles at 2.0 A g^{-1}, it was discovered that the I_2 content retained in the positive electrode had diminished to 71.39% of its initial level, which could be ascribed to tardive I^- dissolution and polyiodide shuttling behaviors. Comparatively, deep-eutectic-LE battery exhibited rapid capacity decay at 5.0 and 2.0 A g^{-1}, attributed to its lower Zn^{2+} transport kinetics, uncontrolled dendrite growth, and electrolyte decomposition. Long-term cycling tests were also conducted at a high I_2 loading of 4.0–5.0 mg cm^{-2} (Supplementary Fig. 23). The Zn|deep-eutectic-HE|I_2 battery similarly demonstrated better electrochemical performances, boasting an initial specific capacity of 144.32 mAh g^{-1} and a capacity retention of 88.35% (average decay: 0.0011% per cycle), which markedly surpasses those of Zn|deep-eutectic-LE|I_2 battery.

The comprehensive rate capability and cycling assessments validate that deep-eutectic-HE delivers high cycling stability and good rate performance in Zn||I_2 full batteries, surpassing conventional HEs. Self-discharge tests were also performed to evaluate the suppression of I^- dissolution and polyiodide shuttling effects in deep-eutectic-HE (Supplementary Fig. 24). After standing for 24 h, the capacity retention of Zn|deep-eutectic-HE|I_2 battery is 93.50%, much higher than that of Zn|deep-eutectic-LE|I_2 battery (80.37%), indicating the improved capability of deep-eutectic-HE

ARTICLE IN PRESS

to inhibit I^- dissolution and polyiodide shuttling.

Temperature resilience tests (Fig. 5d-e) further highlighted the broad temperature adaptability of deep-eutectic-HE. Under −40 °C conditions, the Zn|deep-eutectic-HE|I_2 battery enabled 36,000 cycles with a capacity retention of 92.31% (initial: 97.05 mAh g^{-1}; decay rate: 0.0002%/cycle). At 80 °C, the Zn|deep-eutectic-HE|I_2 battery delivered an initial specific capacity of 146.15 mAh g^{-1} and a capacity retention of 81.00% after 36,000 cycles (decay rate: 0.0002%/cycle). In sharp contrast, deep-eutectic-LE counterparts failed catastrophically within 10 cycles under high temperatures due to frozen electrolyte channels (upon low temperature) and accelerated corrosion (upon high temperature). The broad temperature resilience demonstrated by deep-eutectic-HE under varied temperature conditions (−40 °C to 80 °C) confirms its robust thermomechanical stability and preserves ionic transport characteristics across a wide temperature range. This temperature-adaptive behavior, arising from its synergistic interplay of nanophase separation, hydrated eutectic solvation, and hydrogen-bond networks, established its viability for deployment in geographically diverse environments spanning arctic to desert climates.

Soft-packaged pouch Zn|deep-eutectic-HE|I_2 batteries demonstrated high specific energy of 108.99 Wh kg^{-1} and high volumetric energy density of 189.41 Wh L^{-1} when paired with thicker electrodes, a performance competitive compared to some recent reported zinc-metal batteries (Fig. 5f, Supplementary Fig. 25 and Supplementary Table 8).[69-76] To validate the extensive and universal applicability of deep-eutectic-HE, we also fabricated and tested full battery based on V_2O_5 positive electrode material. The assembled Zn|deep-eutectic-HE|V_2O_5 full battery achieved good energy storage performance, delivering a specific energy of 76.89 Wh kg^{-1} and a volume energy density of 236.62 Wh L^{-1}, both metrics significantly surpassing recent reported zinc-metal batteries. Furthermore, the practical feasibility was validated by three series-connected thinner-than-paper Zn||I_2 batteries that successfully powered a 5×10 light emitting diode (LED) array (3.0 V operational threshold) under demanding conditions, including: (1) severe mechanical deformation (e.g., repeated 180° folding into paper-airplane like origami structures), (2) complete fragmentation via scissor dissection, and (3) cycling under low and high temperatures (−40 °C to

ARTICLE IN PRESS

80 °C), as visualized in Supplementary Fig. 26-27. Even under 90° and 180° bending states, the capacity retention trends of the thinner-than-paper Zn||I_2 pouch batteries during 3,000 cycles are almost identical to the normal unbent state (Supplementary Fig. 28), confirming that the batteries maintain stable electrochemical performances even under significant mechanical deformation, highlighting its potential for practical flexible applications. Moreover, to better demonstrate practical viability, we have integrated three series-connected thinner-than-paper batteries into a watch band for powering a wristwatch, as well as charging a smartphone (Supplementary Fig. 29 and Movie 1-2). These demonstrations highlight the integrability and processability of our electrolyte in more complex and demanding flexible electronic devices.

DISCUSSION

In summary, we report a design of robust deep-eutectic-HE that simultaneously achieves good mechanical stability, high Zn^{2+} conductivity, and broad temperature tolerance. The synergistic effects of nanophase separation, hydrated eutectic solvation, and hydrogen-bond networks endow deep-eutectic-HE with good mechanical properties (4.1 MPa fracture strength and 13.66 MJ m^{-3} toughness) and stable operation from −40 to 80 °C. It effectively regulates Zn^{2+} transport pathways, promoting uniform zinc deposition and suppressing dendrite formation. The resultant materials demonstrate strong mechanical resilience, high ionic conductivity, and broad tolerance to varied temperature conditions. Comprehensive electrochemical and morphological analyses confirm these mechanisms, revealing enhanced cycling durability (36,000 cycles at −40, 20, and 80 °C) and improved rate capability in Zn||I_2 full batteries. The thin thickness of deep-eutectic-HE enables high specific energy and volumetric energy density of 108.99 Wh kg^{-1} and 236.62 Wh L^{-1}, coupled with good flexibility and mechanical durability under demanding conditions. Through the synergistic integration of molecular design, phase modulation, and process engineering, this work develops a practical methodological framework to advance flexible batteries with high energy density and harsh-environment durability for wearable electronics.

ARTICLE IN PRESS

METHODS

Chemicals and materials

$Zn(ClO_4)_2.6H_2O$, urethane (UR), dimethyl sulfoxide (DMSO, 99%), acrylonitrile (AN, 99%), N, N'-methylenebis(acrylamide) (MBA, 99%), ammonium persulfate (APS, 98%), activated carbon (AC, phosphotungstic acid modified), iodine (I_2, 99.99%), vanadium oxide (V_2O_5, 99.99%), N-Methylpyrrolidone (NMP, 99.9%), and lithium iodide (LiI, 99%) were purchased from Aladdin. Polyvinyl alcohol (PVA, M.W. 89,000–98,000, 99% hydrolyzed) was purchased from Sigma Aldrich. Ethanol and acetone were purchased from Wuxi Yasheng Chemical Co., Ltd. Triton X-100 surfactant (10%, Sterile) was purchased from Shanghai Biyun Tian Biotechnology Co., Ltd. Ketjen black (KB, ECP600JD) was purchased from Suzhou Sinero Co., Ltd. Polyvinylidene difluoride (PVDF, 99%) was purchased from Macklin (Shanghai, China). Zinc foils (99.999%, 10–20 μm) were purchased from Shanghai Wenheng Metal Materials Co., Ltd. Cu foils (99.99%, 16 μm) and stainless steel (SS, 316L, 10 μm) foils were purchased from Hefei Kejing Material Co., Ltd. Glass fiber separators (aperture of 2.7 μm) were purchased from Hangzhou Situofan Biotechnology Co., Ltd. Aqueous microporous filtration membranes (0.22 μm) were purchased from Tianjin Jinteng Technology Co., Ltd. All materials were directly used without further purification. Amino-functionalized carbon nanotubes (amino-CNTs, 98%) were purchased from Shenzhen Suiheng Technology Co., Ltd. All metal ingots are used directly without any rolling, surface cleaning, or storing in inert environments treatments.

Preparation of deep-eutectic liquid electrolyte (deep-eutectic-LE) and non-eutectic liquid electrolyte (non-eutectic-LE)

The deep-eutectic-LE sample is prepared by mixing $Zn(ClO_4)_2$, deionized water, and UR in a molar ratio of 1:8:4.5 and stirring at 75 °C for 30 min. The non-eutectic-LE sample is prepared by mixing $Zn(ClO_4)_2$ and deionized water in a 1:8 molar ratio and stirring at 20 °C for 30 min.

Preparation of deep-eutectic hydrogel electrolyte (deep-eutectic-HE) and non-eutectic

ARTICLE IN PRESS

hydrogel electrolyte (non-eutectic-HE)

The deep-eutectic-HE and non-eutectic-HE samples are prepared through a convenient solvent-exchange process. Briefly, a certain amount of PVA powder is dissolved in DMSO under vigorous stirring at 95 °C for about 30 min to obtain a uniform 5 wt.% PVA solution. Subsequently, AN (3 M), MBA (3 mM), and APS (2 mM) are added to the PVA solution under an ice-water bath. Then, the above solution is transferred to a customized mold and copolymerized at 70 °C for 2 h in air isolation, leading to the pristine organogel. Finally, deep-eutectic-HE or non-eutectic-HE sample is prepared by immersing the organogel in deep-eutectic-LE or non-eutectic-LE respectively for 48 h to complete the solvent-exchange between DMSO and deep-eutectic-LE or non-eutectic-LE.

Preparation of positive electrode

The I_2/CNTs positive electrode is prepared by a filtration and adsorption method. Briefly, amino-CNTs (108 mg), AC (12 mg), KB (6 mg), and Triton X-100 surfactant (1 mL) are dissolved in deionized water. Then, the above solution is subjected to ultrasonic dispersion treatment in an ice-water bath for 200 min using an ultrasonic cell disruptor to obtain a uniform mixture solution. Next, the above solution is vacuum filtered via an aqueous microporous filtration membrane. Afterwards, the filtration membrane is dissolved and washed by acetone, and the resulting CNTs film with a thickness of 20–200 μm is dried in a vacuum oven at 80 ºC for 24 h. The obtained self-supporting CNTs film is stamped into circular electrode plates with a diameter of 10 mm. Subsequently, the CNTs film electrode is immersed in an ethanol solution of 0.1 M I_2 for 24 h to fully adsorb I_2 into the CNTs film electrode (I_2/CNTs). Finally, the I_2/CNTs electrode is transferred to a vacuum oven and dried at 80 ºC for 24 h to obtain the I_2/CNTs positive electrode. The loading amount of I_2 active material is varied to be about 0.5–1.5 mg cm^{-2} (unless otherwise noted), 4.0–5.0 mg cm^{-2} (for high I_2 loading tests), or 18–22 mg cm^{-2} (for the assembly of soft-packed batteries), which is determined by the thickness of CNTs film. All I_2/CNTs positive electrodes are used directly without any rolling, surface cleaning, or storing in inert environments treatments.

The V_2O_5 positive electrode is prepared using a scratch coating method. Briefly, 140 mg of V_2O_5,

ARTICLE IN PRESS

40 mg of KB, and 20 mg of PVDF (with a mass ratio of 7:2:1) were evenly ground with a agate mortar, and mixed with NMP, and stirred for 24 h to form a uniform slurry. The slurry is coated on a SS foil (thickness of 10 μm) with a stainless-steel scraper and dried in a vacuum oven at 60 ºC for 24 h. After drying, the V_2O_5 positive electrode is rolled by a roller machine with a pressure of 10 MPa. The active mass loading is 19–22 mg cm^{-2}. All V_2O_5 positive electrodes are used directly without any surface cleaning or storing in inert environments treatments.

Material characterizations

Attenuated total reflection Fourier transform infrared (ATR-FTIR) spectra are collected using a Thermo Fisher Scientific Nicolet iS10. Raman spectra ware collected using a Horiba JY Raman spectrometer equipped with a 473 nm laser light source. Scanning electron microscopy (SEM) images are obtained using FEI Nova NanoSEM-450 field emission scanning electron microscopy. The 2D and 3D topographies of the samples are observed with a Bruker Dimension Icon atomic force microscopy (AFM) instrument. The optical transmittance measurements are measured via a Shimadzu UV-2700 UV-vis-NIR spectrophotometer. X-ray diffraction (XRD) data is obtained using a Bruker D8 ADVANCE powder X-ray diffractometer. Small angle X-ray scattering (SAXS) data are measured on the Xeuss 2.0 SAXS system. The mechanical properties are measured using an Instron 3343 instrument. Differential scanning calorimetry (DSC) tests are conducted using a PerkinElmer Pyris 1 analyzer. The rheological tests are performed on a TA DHR-2 rheometer. The temperature-dependent sweeps are conducted ranging from 10 to 100 °C at 0.1% strain and 5 rad s^{-1}. The moisture retention rate is tested by drying method. Specifically, a standard cylindrical sample is exposed to an environment of 25 °C and 15% relative humidity (RH). During this process, the weight of the sample is regularly measured, and the water retention of the sample over time is calculated using Equation (1), as provided below. The percentage content of I_2 in the electrode is evaluated via thermogravimetric (TG) analysis on a Netzsch STA 449C thermal analyzer with a heating rate of 10 °C min^{-1} from 30 to 500 °C under a dry air atmosphere. Some electrodes and electrolytes are directly characterized after preparation, while others are obtained from aqueous

ARTICLE IN PRESS

batteries after specific electrochemical tests. In the air environment, stainless-steel pliers are used for disassembling CR2032 batteries, and stainless-steel tweezers are used to transfer electrodes and electrolytes. After transferring from the battery, the negative electrodes are rinsed with deionized water and dried at 60 °C before further characterization, while positive electrodes and electrolytes are dried without rinsed. The inert atmosphere has never been used.

Fabrication of the batteries

The electrochemical performances of LE and HE samples are evaluated using CR2032 batteries or soft-packaged pouch batteries. The SS||SS symmetrical batteries are composed of two SS foils (diameter of 12 mm, thickness of 10 μm) and a specific electrolyte. The Zn||Zn symmetrical batteries are composed of two Zn foils (diameter of 12 mm, thickness of 10 μm) and a specific electrolyte. The Zn||Cu half batteries are composed of a Zn foil negative electrode (diameter of 12 mm, thickness of 10 μm), a Cu foil positive electrode (diameter of 12 mm, thickness of 16 μm), and a specific electrolyte. The Zn||SS half batteries are composed of a Zn foil negative electrode (diameter of 12 mm, thickness of 10 μm), a SS foil positive electrode (diameter of 12 mm, thickness of 10 μm), and a specific electrolyte. The Zn||I_2 CR2032 batteries are composed of a Zn foil negative electrode (diameter of 12 mm, thickness of 10 μm), a I_2 positive electrode (diameter of 12 mm, thickness of 20 μm), and a specific electrolyte. The single layer Zn||I_2 soft-packaged pouch batteries are composed of a layer of Zn foil negative electrode (5.0 cm × 4.0 cm, thickness of 10 μm), a layer of I_2 positive electrode (5.0 cm × 4.0 cm, thickness of 20 μm, active mass loading of 1.0–1.5 mg cm^{-2} or 4.0–5.0 mg cm^{-2}), and a layer of deep-eutectic-HE (6.0 cm × 5.0 cm, thickness of 10 μm). The multi-layer Zn||I_2 soft-packaged pouch batteries are composed of 11 layers of Zn foil negative electrodes (5.0 cm × 4.0 cm, thickness of 10 μm), 10 layers of I_2 positive electrodes (5.0 cm × 4.0 cm, thickness of 190±10 μm, active mass loading of 18–22 mg cm^{-2}), and 20 layers of deep-eutectic-HEs (6.0 cm × 5.0 cm, thickness of 10 μm). The multi-layer Zn||V_2O_5 soft-packaged pouch batteries are composed of 11 layers of Zn foil negative electrodes (5.0 cm × 4.0 cm, thickness of 15 μm), 10 layers of V_2O_5 positive electrodes (double-side coated, 5.0 cm ×

ARTICLE IN PRESS

4.0 cm, thickness of 100±10 μm, active mass loading of 19–22 mg cm^{-2}), and 20 layers of deep-eutectic-HEs (6.0 cm × 5.0 cm, thickness of 10 μm).

The diameter, thickness and shell material of the above-mentioned CR2032 battery are 20 mm, 3.2 mm, and stainless steel, respectively. The above-mentioned soft-packaged pouch batteries are packaged with polyimide films (thickness of 3 μm) under a vacuum condition, without applying external pressure during the charging/discharging cycling process. The above-mentioned electrolytes refer to deep-eutectic-HE (without any separator), deep-eutectic-LE (with glass fiber separators), non-eutectic-HE (without any separator), or non-eutectic-LE (with glass fiber separators). The thickness of deep-eutectic-HE, non-eutectic-HE and glass fiber separator are 10 μm, 100 μm and 250 μm, respectively. The size of deep-eutectic-HE, non-eutectic-HE and glass fiber separator used in CR2032 batteries are 16 mm in diameters. The size of deep-eutectic-HEs used in soft-packaged pouch batteries are 5.5 cm × 4.5 cm. All electrolytes are used within 7 days after preparation, storing in glass bottles (LEs) and cling films (HEs) under air atmosphere (20±2 °C). LEs and HEs are transferred with a pipettor (polypropylene pipette tip) and a stainless-steel tweezer under air atmosphere (20±2 °C), respectively. The glass fiber separators are cut with a stainless-steel circular slicer and are directly wetted by dripping electrolyte during battery assembly instead of prewetting. The negative/positive ratio (N/P) of the above-mentioned Zn||I_2 coin batteries, Zn||I_2 soft-packaged pouch batteries and Zn||V_2O_5 soft-packaged pouch batteries are calculated to be 18.50–55.50 or 5.55–6.94, 1.26–1.54 and 1.35–1.57 (based on the active mass loading of positive electrodes).

Electrochemical measurements

The cyclic voltammetry (CV), linear sweep voltammetry (LSV), alternating-current electrochemical impedance spectroscopy (EIS), chronoamperometry (CA), and Tafel curves are collected on RST-5200F and CHI-760 electrochemical workstations at 20±2 °C. The CV and LSV tests are performed at a scan rate of 1.0 mV s^{-1}, with a potential range of −0.2–0.4 V and 1.0–3.0 V (vs. Zn/Zn^{2+}), respectively. The EIS tests are performed with an amplitude of 5 mV in the

ARTICLE IN PRESS

frequency range between 100 kHz and 0.01 Hz at 20±2 °C. The measurement is conducted after holding the batteries at the specified temperature for 1 h during open-circuit potential. Nyquist plots obtained from EIS tests are fitted using ZView software. The CA tests are conducted after EIS tests immediately with a polarization voltage of 10 mV and a discharging time of 600 seconds. The Tafel curves are collected at the scanning rate of 1 mV s^{-1} across a voltage range of ±180 mV relative to the open-circuit voltage.

Galvanostatic charge/discharge cycling tests and rate performance measurements are conducted on a NEWARE CT-4008Tn battery analyzer using constant current techniques in a incubator (−40±2 °C, 20±2 °C or 80±2 °C). The Zn||Zn symmetrical batteries are tested at the current density ranging from 0.5–5.0 mA cm^{-2} with an area capacity of 0.5 mAh cm^{-2}. The average Coulomb efficiency is measured with the Zn||Cu half batteries using the following procedure: a discharging process is first performed at a current density of 0.5 mA cm^{-2} for 1 hour. Then, 20 charging/discharging cycles are performed at 0.5 mA cm^{-2} with an area capacity of 0.5 mAh cm^{-2}. Finally, the battery is charged to 0.5 V (vs. Zn/Zn^{2+}) at a current density of 0.5 mA cm^{-2}. The average Coulombic efficiency is then calculated via Equation 4**.** The Zn||I_2 batteries are tested at the current density ranging from 0.5–10.0 A g^{-1} with a discharging cut-off potential of 0.7 V (vs. Zn/Zn^{2+}) and a charging cut-off potential of 1.5 V (vs. Zn/Zn^{2+}). The Zn||V_2O_5 batteries are tested at the current density of 0.5 A g^{-1} (based on the mass of V_2O_5 positive electrode active materials) with a discharging cut-off potential of 0.2 V (vs. Zn/Zn^{2+}) and a charging cut-off potential of 1.6 V (vs. Zn/Zn^{2+}). All electrochemical tests are conducted in a gas environment of air. No local temperature measurements are carried out. The specific capacities and current density of Zn||I_2 and Zn||V_2O_5 batteries are calculated according to the mass of positive electrode active materials.

All electrochemical measurements are repeated at least 3 times to ensure statistical reliability and reproducibility. The values of ionic conductivity (5 repetitions) and Zn^{2+} transference number (5 repetitions) reflect statistical analysis of all tested batteries in parallel experiments, as these tests allow high-throughput measurement under identical conditions, and enable rigorous error quantification critical for characterization. Conversely, the CV (3 repetitions), LSV (3 repetitions),

ARTICLE IN PRESS

Tafel (3 repetitions) and long-cycling performance (3-5 repetitions) data presented in the figures represent measurements from a specific representative battery selected from multiple identical experiments (exhibited median performance in several repetitions). This approach is adopted because a single battery can display its detailed electrochemical performance in a complete curve, while the statistical analysis inevitably loses some critical information, especially the large amount of data of galvanostatic charge/discharge cycling tests (over 1000 cycles).

Calculation equations

The water retention (W_r) is calculated according to the following equation:

$$W_r = \frac{W_s}{W_0} \times 100\% \quad \text{Equation (1)}$$

where W_0 and W_s are the mass of the sample after exposure for 0 and s h, respectively.

The ionic conductivity (σ) is calculated according to the following equation:

$$\sigma = \frac{l}{R \cdot S} \quad \text{Equation (2)}$$

where l and S represent the thickness and area of the electrolyte, respectively. R is the bulk resistance of the electrolyte.

The Zn-ion transference number ($t_{Zn^{2+}}$) is calculated according to the following equation:

$$t_{Zn^{2+}} = \frac{I_S(\Delta V - I_0 R_{el}^0)}{I_0(\Delta V - I_S R_{el}^S)} \quad \text{Equation (3)}$$

where ΔV is the polarization voltage (30 mV), I_0 and I_s are the initial current and steady current, respectively. R_{el}^0 and R_{el}^s are the initial interfacial resistance and steady interfacial resistance, respectively.

The average Coulombic efficiency (CE_{avg}) during the Zn plating/stripping process in Zn||Cu half batteries is calculated according to the following equation:

$$CE_{avg} = 1 - \frac{Q_1 - Q_r}{Q_c N} \quad \text{Equation (4)}$$

where Q_1 is the initial Zn plating capacity (5.0 mAh cm^{-2}), Q_r is the capacity retention measured by the final Zn stripping process, Q_c is the fixed plating or striping capacity (0.5 mAh cm^{-2}) involved in a single plating or stripping process (half cycle), and N is the cycling number of

ARTICLE IN PRESS

plating/stripping process.

The percentage content of I_2 in the electrode (M_{I_2}) is calculated according to the following equation:

$$M_{I_2} = \frac{M_{I_2+C+H_2O} - M_{C+H_2O}}{1 - M_{C+H_2O}} \quad \text{Equation (5)}$$

where $M_{I_2+C+H_2O}$ and M_{C+H_2O} are the weight loss of electrodes containing I_2 and electrodes without I_2 in TG tests, respectively.

The percentage content of I_2 retained in the positive electrode (I_2 remained) is calculated according to the following equation:

$$I_2 \text{ remained} = \frac{M_{After}(1 - M_{Before})}{M_{Before}(1 - M_{After})} \quad \text{Equation (6)}$$

where M_{Before} and M_{After} are the percentage content of I_2 in the positive electrode before and after charging/discharging cycling tests, respectively.

The standard deviation (SD) of the samples is calculated according to the following equation:

$$SD = \sqrt{\frac{\sum_{i=1}^{n} x_i - \bar{x}}{n-1}} \quad \text{Equation (7)}$$

where x_i, $\bar{x}$, and n are the i-th sample data, sample mean, and sample size, respectively. All error bars mentioned in the text represent SD.

The specific capacity of the batteries is calculated according to the following equation:

$$\text{Specific capacity} = \frac{C}{M_p} \quad \text{Equation (8)}$$

where C and M_p are the capacity (mAh) and mass (g) of the positive electrode active materials, respectively.

The specific energy of the batteries is calculated according to the following equation:

$$\text{Specific energy} = \frac{E}{M} \quad \text{Equation (9)}$$

where E and M are the total energy (Wh) and total mass (kg) of the battery, respectively.

The volumetric energy density of the batteries is calculated according to the following equation:

$$\text{Volumetric energy density} = \frac{E}{V} \quad \text{Equation (10)}$$

where E and V are the total energy (Wh) and total volume (L) of the battery, respectively.

ARTICLE IN PRESS

Theoretical simulations

All theoretical calculations are performed using Materials Studio. The geometric structures and binding energies between PAN, PVA, UR, H_2O, and $Zn(ClO_4)_2$ are optimized using the DMol3 module. The gradient approximation (GGA) of the Perdew-Burke-Ernzerh (PBE) functional is used to describe electron exchange and associated energy. Density functional theory (DFT) - D3 method is used in the calculation to consider van der Waals forces. The plane wave cutoff energy is set to 520 eV, and the energy convergence value between two consecutive steps is less than 10^{-5} eV. The maximum allowable force is less than 0.002 eV/Å, and the maximum allowable displacement is less than 0.005 Å.

Four electrolyte models are constructed to simulate four as-prepared electrolytes: deep-eutectic-HE, deep-eutectic-LE, non-eutectic-HE, and non-eutectic-LE, respectively. Molecular dynamics (MD) simulations are performed on four electrolyte models using the Forcite module. The Condensed Phase Optimized Molecular Potential (COMPASS III) force field is selected for atomic simulation studies for all MD simulations. For each system, the isothermal isobaric ensemble (NPT) is first used to pre-equilibrate the system for 1 ns. Then, a 5 ns MD run is performed in the canonical ensemble (NVT) to achieve equilibrium, followed by a 5 ns NVT simulation to obtain the final electrolyte model. The time step of the MD simulation process mentioned above is set to 1 fs.

ARTICLE IN PRESS

DATA AVAILABILITY

The authors declare that all data supporting the finding of this study are available within the paper and its Supplementary Information. Source data are provided with this paper.

REFERENCES

1. Hongyu Lu, Jisong Hu, Xijun Wei, Kaiqi Zhang, Xiao Xiao, Jingxin Zhao, Qiang Hu, Jing Yu, Guangmin Zhou, Bingang Xu, A recyclable biomass electrolyte towards green zinc-ion batteries, *Nat. Commun.* **14**, 4435 (2023).

ARTICLE IN PRESS

2. Chongyin Yang, Jiale Xia, Chunyu Cui, Travis P. Pollard, Jenel Vatamanu, Antonio Faraone, Joseph A. Dura, Madhusudan Tyagi, Alex Kattan, Elijah Thimsen, Jijian Xu, Wentao Song, Enyuan Hu, Xiao Ji, Singyuk Hou, Xiyue Zhang, Michael S. Ding, Sooyeon Hwang, Dong Su, Yang Ren, Xiaoqing Yang, Howard Wang, Oleg Borodin, Chunsheng Wang, All-temperature zinc batteries with high-entropy aqueous electrolyte, *Nat. Sustain.* **6**, 325-335 (2023).
3. Wei Chen, Guodong Li, Allen Pei, Yuzhang Li, Lei Liao, Hongxia Wang, Jiayu Wan, Zheng Liang, Guangxu Chen, Hao Zhang, Jiangyan Wang, Yi Cui, A manganese-hydrogen battery with potential for grid-scale energy storage, *Nat. Energy* **3**, 428-435 (2018).
4. Ben Niu, Jia Wang, Yalan Guo, Zhengang Li, Chengyao Yuan, Anqi Ju, Xin Wang, Polymers for aqueous zinc-ion batteries: From fundamental to applications across core components, *Adv. Energy Mater.* **14**, 2303967 (2024).
5. Ruiyu Qi, Wenhao Tang, Yiliang Shi, Kewei Teng, Yirui Deng, Lei Zhang, Junqing Zhang, Ruiping Liu, Gel polymer electrolyte toward large-scale application of aqueous zinc batteries, *Adv. Funct. Mater.* **33**, 2306052 (2023).
6. Peng Yang, Kai Zhang, Shizhuo Liu, Wubin Zhuang, Zhipeng Shao, Kaiping Zhu, Lin Lin, Gengde Guo, Wenhui Wang, Qichong Zhang, Yagang Yao, Ionic selective separator design enables long-life zinc-iodine batteries via synergistic anode stabilization and polyiodide shuttle suppression, *Adv. Funct. Mater.* **34**, 2410712 (2024).
7. Xiao Xiao, Zhiyang Zheng, Xiongwei Zhong, Runhua Gao, Zhihong Piao, Miaolun Jiao, Guangmin Zhou, Rational design of flexible Zn-based batteries for wearable electronic devices, *ACS Nano* **17**, 1764-1802 (2023).
8. Mingjie Wu, Gaixia Zhang, Huaming Yang, Xianhu Liu, Marc Dubois, Marc A. Gauthier, Shuhui Sun, Aqueous Zn-based rechargeable batteries: Recent progress and future perspectives, *InfoMat* **4**, e12265 (2021).
9. Zhiyang Lyu, Gwendolyn J.H. Lim, J. Justin Koh, Yi Li, Yanwen Ma, Jun Ding, Jinlan Wang, Zheng Hu, John Wang, Wei Chen, Yunfei Chen, Design and manufacture of 3D-printed

ARTICLE IN PRESS

batteries, *Joule* **5**, 89-114 (2021).

10. Yanbo Wang, Qing Li, Hu Hong, Shuo Yang, Rong Zhang, Xiaoqi Wang, Xu Jin, Bo Xiong, Shengchi Bai, Chunyi Zhi, Lean-water hydrogel electrolyte for zinc ion batteries, *Nat. Commun.* **14**, 3890 (2023).
11. Fusheng Luo, Song Yang, Qing Wu, Yue Li, Jinlong Zhang, Yanhui Zhang, Jun Huang, Haibo Xie, Yiwang Chen, Hydrogel electrolytes with an electron/ion dual regulation mechanism for highly reversible flexible zinc batteries, *Energy Environ. Sci.* **17**, 8570-8581 (2024).
12. Doudou Feng, Yucong Jiao, Peiyi Wu, Guiding Zn uniform deposition with polymer additives for long-lasting and highly utilized Zn metal anodes, *Angew. Chem. Int. Ed.* **62**, e202314456 (2023).
13. Xiangye Li, Dahui Wang, Fen Ran, Key approaches and challenges in fabricating advanced flexible zinc-ion batteries with functional hydrogel electrolytes, *Energy Storage Mater.* **56**, 351-393 (2023).
14. Zijian Hong, Zeeshan Ahmad, Venkatasubramanian Viswanathan, Design principles for dendrite suppression with porous polymer/aqueous solution hybrid electrolyte for Zn metal anodes, *ACS Energy Lett.* **5**, 2466-2474 (2020).
15. Chaowei Li, Wenhui Wang, Jie Luo, Wubin Zhuang, Jianxian Zhou, Shizuo Liu, Lin Lin, Wenbin Gong, Guo Hong, Zhipeng Shao, Jimin Du, Qichong Zhang, Yagang Yao, High-fluidity/high-strength dual-layer gel electrolytes enable ultra-flexible and dendrite-free fiber-shaped aqueous zinc metal battery, *Adv. Mater.* **36**, 2313772 (2024).
16. Zongju Chen, Tianyu Shen, Minhao Zhang, Xiong Xiao, Hongqin Wang, Qingru Lu, Yanlong Luo, Zhong Jin, Chenghui Li, Tough, anti-fatigue, self-adhesive, and anti-freezing hydrogel electrolytes for dendrite-free flexible zinc ion batteries and strain sensors, *Adv. Funct. Mater.* **34**, 2314864 (2024).
17. Cheng Tang, Yinzhuo Yao, Manni Li, Yaling Wang, Yan Zhang, Jian Zhu, Ling Wang, Lei Li, A new polyvinyl alcohol lithium chloride hydrogel electrolyte: high ionic conductivity and wide working temperature range, *Adv. Funct. Mater.* **35**, 2417207 (2025).

ARTICLE IN PRESS

18. Huan Xia, Gang Xu, Xin Cao, Chunyang Miao, Hanning Zhang, Pengyu Chen, Yang Zhou, Wei Zhang, Zhengming Sun, Single-ion-conducting hydrogel electrolytes based on slide-ring pseudo-polyrotaxane for ultralong-cycling flexible zinc-ion batteries, *Adv. Mater.* **35**, 2301996 (2023).
19. Xilin Wang, Bin Wang, Jianli Cheng, Multi-Healable, Mechanically Durable Double Cross-Linked Polyacrylamide Electrolyte incorporating hydrophobic interactions for dendrite-free flexible zinc-ion batteries, *Adv. Funct. Mater.* **33**, 2304470 (2023).
20. Jingran Zhang, Chuyuan Lin, Lingxing Zeng, Hui Lin, Lingjun He, Fuyu Xiao, Luteng Luo, Peixun Xiong, Xuhui Yang, Qinghua Chen, Qingrong Qian, A hydrogel electrolyte with high adaptability over a wide temperature range and mechanical stress for long-life flexible zinc-ion batteries, *Small* **20**, 2312116 (2024).
21. Gayoung Shim, Minh Xuan Tran, Guicheng Liu, Dongjin Byun, Joong Kee Lee, Flexible, fiber-shaped, quasi-solid-state Zn-polyaniline batteries with methanesulfonic acid-doped aqueous gel electrolyte, *Energy Storage Mater.* **35**, 739-749 (2021).
22. Jing Xu, Haolin Li, Yang Jin, Dong Zhou, Bing Sun, Michel Armand, Guoxiu Wang, Understanding the electrical mechanisms in aqueous zinc metal batteries: From electrostatic interactions to electric field regulation, *Adv. Mater.* **36**, 2309726 (2024).
23. Yichen Yan, Sidi Duan, Bo Liu, Shuwang Wu, Yousif Alsaid, Bowen Yao, Sunny Nandi, Yingjie Du, Ta-Wei Wang, Yuzhang Li, Ximin He, Tough hydrogel electrolytes for anti-freezing zinc-ion batteries, *Adv. Mater.* **35**, 2211673 (2023).
24. Hongyu Lu, Jisong Hu, Litong Wang, Jianzhu Li, Xiang Ma, Zhicheng Zhu, Heqi Li, Yingjie Zhao, Yujie Li, Jingxin Zhao, Bingang Xu, Multi-component crosslinked hydrogel electrolyte toward dendrite-free aqueous Zn ion batteries with high temperature adaptability, *Adv. Funct. Mater.* **32**, 2112540 (2022).
25. Yanyan Shao, Jin Zhao, Wenguang Hu, Zhou Xia, Jinrong Luo, Yijing Zhou, Liang Zhang, Xianzhong Yang, Ning Ma, Dongzi Yang, Qiuwei Shi, Jingyu Sun, Lei Zhang, Jingshu Hui, Yuanlong Shao, Regulating interfacial ion migration via wool keratin mediated biogel

ARTICLE IN PRESS

electrolyte toward robust flexible Zn-ion batteries, *Small* **18**, 2107163 (2022).

26. Minfeng Chen, Jizhang Chen, Weijun Zhou, Xiang Han, Yagang Yao, Ching-Ping Wong, Realizing an all-round hydrogel electrolyte toward environmentally adaptive dendrite-free aqueous Zn-MnO_2 batteries, *Adv. Mater.* **33**, 2007559 (2021).
27. Qing Li, Donghong Wang, Boxun Yan, Yuwei Zhao, Jun Fan, Chunyi Zhi, Dendrite issues for zinc anodes in a flexible cell configuration for zinc-based wearable energy-storage devices, *Angew. Chem. Int. Ed.* **61**, e202202780 (2022).
28. Zhiming Zhao, Jinzhi Wang, Zhaolin Lv, Qinglei Wang, Yaojian Zhang, Guoli Lu, Jingwen Zhao, Guanglei Cui, In-situ formed all-amorphous poly (ethylene oxide)-based electrolytes enabling solid-state Zn electrochemistry, *Chem. Eng. J.* **417**, 128096 (2021).
29. Peihua Yang, Chunzao Feng, Yipu Liu, Ting Cheng, Xuelong Yang, Huidong Liu, Kang Liu, Hong Jin Fan, Thermal self-protection of zinc-ion batteries enabled by smart hygroscopic hydrogel electrolytes, *Adv. Energy Mater.* **10**, 2002898 (2020).
30. Zongju Chen, Tianyu Shen, Xiong Xiao, Xiuchong He, Yanlong Luo, Zhong Jin, Chenghui Li, An ultrahigh-modulus hydrogel electrolyte for dendrite-free zinc ion batteries, *Adv. Mater.* **36**, 2413268 (2024).
31. Yongchuan Wu, Ya Zhang, Haidi Wu, Jing Wen, Shu Zhang, Wenqian Xing, Hechuan Zhang, Huaiguo Xue, Jiefeng Gao, Yiuwing Mai, Solvent-exchange-assisted wet annealing: A new strategy for superstrong, tough, stretchable, and anti-fatigue hydrogels, *Adv. Mater.* **35**, 2210624 (2023).
32. Rumin Fu, Lingjie Tu, Yahong Zhou, Lei Fan, Fengmiao Zhang, Zhengao Wang, Jun Xing, Dafu Chen, Chunlin Deng, Guoxin Tan, Peng Yu, Lei Zhou, Chengyun Ning, A tough and self-powered hydrogel for artificial skin, *Chem. Mater.* **31**, 9850-9860 (2019).
33. Hongbo Wan, Baohu Wu, Lei Hou, Peiyi Wu, Amphibious polymer materials with high strength and superb toughness in various aquatic and atmospheric environments, *Adv. Mater.* **36**, 2307290 (2024).

ARTICLE IN PRESS

ARTICLE IN PRESS

34. Guanghua Cao, Lei Zhao, Xiwei Ji, Yuanyou Peng, Meimei Yu, Xiangya Wang, Xiangye Li, Fen Ran, “Salting out” in hofmeister effect enhancing mechanical and electrochemical performance of amide-based hydrogel electrolytes for flexible zinc-ion battery, *Small* **19**, 2207610 (2023).
35. Desheng Liu, Yufei Cao, Pan Jiang, Yixian Wang, Yaozhong Lu, Zhongying Ji, Xiaolong Wang, Weimin Liu, Tough, transparent, and slippery PVA hydrogel led by syneresis, *Small* **19**, 2206819 (2023).
36. Xule Yang, Liju Xu, Chen Wang, Jilin Wu, Bin Zhu, Xiaohui Meng, Dong Qiu, Reinforcing hydrogel by nonsolvent-quenching-facilitated in situ nanofibrosis, *Adv. Mater.* **35**, 2303728 (2023).
37. Guanghua Cao, Lei Zhao, Xiwei Ji, Yuanyou Peng, Meimei Yu, Xiangya Wang, Xiangye Li, Fen Ran, “Salting out” in Hofmeister effect enhancing mechanical and electrochemical performance of amide-based hydrogel electrolytes for flexible zinc-ion battery, *Small* **19**, 2207610 (2023).
38. Guoqun Zhang, Lulu Fu, Yuan Chen, Kun Fan, Chenyang Zhang, Huichao Dai, Linnan Guan, Minglei Mao, Jing Ma, Chengliang Wang, Hofmeister effects in supramolecular chemistry for anion-modulation to stabilize Zn anode, *Adv. Mater.* **36**, 2405949 (2024).
39. Ning Tang, Yujia Jiang, Kailun Wei, Zhiran Zheng, Hao Zhang, Jun Hu, Evolutionary reinforcement of polymer networks: a stepwise-enhanced strategy for ultrarobust eutectogels, *Adv. Mater.* **36**, 2309576 (2024).
40. Guoshen Yang, Jialei Huang, Xuhao Wan, Binbin Liu, Yachao Zhu, Jiawei Wang, Olivier Fontaine, Shiqiang Luo, Pritesh Hiralal, Yuzheng Guo, Hang Zhou, An aqueous zinc-ion battery working at −50 °C enabled by low-concentration perchlorate-based chaotropic salt electrolyte, *EcoMat* **4**, e12165 (2022).
41. Jaeil Park, Jongyoon Kim, Subin Lee, Ji Hwan Kim, Myung-Han Yoon, Dongwook Lee, Seung Joon Yoo, Unraveling concentration-dependent solvation structures and molecular

ARTICLE IN PRESS

interactions in water-in-salt electrolytes for enhanced performance of electric double-layer capacitors, *Energy Storage Mater.* **65**, 103137 (2024).

42. Benjamin Malfait, Aicha Jani, Denis Morineau, Confining deep eutectic solvents in nanopores: Insight into thermodynamics and chemical activity, *J. Mol. Liq.* **349**, 118488 (2022).
43. Meijia Qiu, Yuxuan Liang, Jiahong Hong, Jiale Li, Peng Sun, Wenjie Mai, Entropy-driven hydrated eutectic electrolytes with diverse solvation configurations for all-temperature Zn-ion batteries, *Angew. Chem. Int. Ed.* **63**, e202407012 (2024).
44. Lu Yao, Chenxin Hou, Mingqiang Liu, Haibiao Chen, Qinghe Zhao, Yan Zhao, Yuetao Wang, Lele Liu, Zu-Wei Yin, Jimin Qiu, Shunning Li, Runzhi Qin, Feng Pan, Ultra-stable Zn anode enabled by fiber-directed ion migration using mass-producible separator, *Adv. Funct. Mater.* **33**, 2209301 (2022).
45. Yishu Li, Xiaodan Yang, Yan He, Fan Li, Kefeng Ouyang, Dingtao Ma, Juan Feng, Jiali Huang, Jinlai Zhao, Ming Yang, Yanyi Wang, Yangsu Xie, Hongwei Mi, Peixin Zhang, A novel ultrathin multiple-kinetics-enhanced polymer electrolyte editing enabled wide-temperature fast-charging solid-state zinc metal batteries, *Adv. Funct. Mater.* **34**, 2307736 (2023).
46. Xinyu Zhao, Huidong Xu, Zhao-Tie Liu, Guo Li, Jinqiang Jiang, Zhong-Wen Liu, Designable polypyrrole pattern in hydrogel achieved by photo-controllable concentration of Fe^{3+} initiator, *Smart Mol.* **2**, e20240015 (2024).
47. Xiong Xiao, Zongju Chen, Russell J. Varley, Chenghui Li, Smart bistable coordination complexes, *Smart Mol.* **2**, e20230028 (2024).
48. James Kumankuma-Sarpong, Caiyun Chang, Jing Hao, Titi Li, Xianming Deng, Cuiping Han, Baohua Li, Entanglement added to cross-linked chains enables tough gelatin-based hydrogel for Zn metal batteries, *Adv. Mater.* **36**, 2403214 (2024).
49. Qinbo Liu, Junfu Li, Doudou Xing, Yingjie Zhou, Feng Yan, Ternary eutectic electrolyte for flexible wide-temperature zinc-ion batteries from −20 °C to 70 °C, *Angew. Chem. Int. Ed.* **64**, e202414728 (2025).

ARTICLE IN PRESS

50. Shaojie Guo, Mengyu Yan, Dongming Xu, Pan He, Kaijian Yan, Jiexin Zhu, Yongkun Yu, Zeya Peng, Yanzhu Luo, Feifei Cao, Anti-freezing hydrogel electrolyte with a regulated hydrogen bond network enables high-rate and long cycling zinc batteries, *Energy Environ. Sci.* **18**, 418-429 (2025).
51. Yingxiang Huang, Yanzhao Yang, Cong Peng, Yu Li, Wei Feng, High strength, strain, and resilience of gold nanoparticle reinforced eutectogels for multifunctional sensors, *Adv. Sci.* **12**, 2416318 (2025).
52. Yafen Zheng, Dongling Wu, Tao Wang, Qian Liu, Dianzeng Jia, Advanced eutectogel electrolyte for high-performance and wide-temperature flexible zinc-air batteries, *Angew. Chem. Int. Ed.* **64**, e202418223 (2024).
53. Yongqi Deng, Yihan Wu, Kefu Zhang, Minghui Fan, Lele Wang, Yapeng Hea, Lifeng Yan, Inhibition of side reactions and dendrite growth using a low-cost and non-flammable eutectic electrolyte for high-voltage and super-stable zinc hybrid batteries, *J. Mater. Chem. A* **11**, 8368-8379 (2023).
54. Zhouquan Sun, Yunhao Hu, Wei Wei, Yaogang Li, Qinghong Zhang, Kerui Li, Hongzhi Wang, Chengyi Hou, Hyperstable eutectic core-spun fiber enabled wearable energy harvesting and personal thermal management fabric, *Adv. Mater.* **36**, 2310102 (2023).
55. Jichao Zhai, Wang Zhao, Lei Wang, Jianbo Shuai, Ruwei Chen, Wenjiao Ge, Yu Zong, Guanjie He, Xiaohui Wang, Ultrathin cellulosic gel electrolytes with a gradient hydropenic interface for stable, high-energy and flexible zinc batteries, *Energy Environ. Sci.* **18**, 4241-4250 (2025).
56. Huan Xia, Wei Zhang, Chunyang Miao, Hao Chen, Chengjie Yi, Yihan Shang, Tao Shui, Xin Cao, Jiacheng Liu, Song-Zhu Kure-Chu, Feifei Liang, Nosipho Moloto, Yipeng Xiong, Takehiko Hihara, Weibing Lu, ZhengMing Sun, Ultra-thin amphiphilic hydrogel electrolyte for flexible zinc-ion paper batteries, *Energy Environ. Sci.* **17**, 6507-6520 (2024).
57. Xiao Zhang, Jiayi Li, Fengjin Xie, Xinming Xu, Xunzhen Sun, Long Su, Fei Lu, Liqiang Zheng, Xinpei Gao, Polyzwitterionic gel electrolyte: dual optimization of polyiodide shuttle

ARTICLE IN PRESS

suppression and anode stabilization in aqueous Zn-I_2 batteries, *Adv. Funct. Mater.* **35**, 2505132 (2025).

58. Yadong Tian, Song Chen, Siyu Ding, Qianwu Chen, Jintao Zhang, A highly conductive gel electrolyte with favorable ion transfer channels for long-lived zinc–iodine batteries, *Chem. Sci.* **14**, 331-337 (2023).
59. Xuan Zhou, Song Huang, Liang Gao, Zicheng Zhang, Qinyang Wang, Zuyang Hu, Xiaoting Lin, Yulong Li, Zequn Lin, Yufei Zhang, Yongchao Tang, Zhipeng Wen, Minghui Ye, Xiaoqing Liu, Cheng Chao Li, Molecular bridging induced anti-salting-out effect enabling high ionic conductive $ZnSO_4$-based hydrogel for quasi-solid-state zinc ion batteries, *Angew. Chem. Int. Ed.* **63**, e202410434 (2024).
60. Doron Aurbach, Yosef Gofer, Jacob Langzam, The correlation between surface chemistry, surface morphology, and cycling efficiency of lithium electrodes in a few polar aprotic systems, *J. Electrochem. Soc.* **136**, 3198 (1989).
61. Yuhan Chen, Jianan Yin, Yaqin Zhang, Fucong Lyu, Bin Qin, Jingwen Zhou, Jia-Hua Liu, Yun-Chen Long, Zhengyi Mao, Mulin Miao, Xiaoqiang Cai, Jun Fan, Jian Lu, Coupling high hardness and Zn affinity in amorphous-crystalline diamond for stable Zn metal anodes, *ACS Nano* **18**, 14403-14413 (2024).
62. Ruijie Zhu, Huijun Yang, Wei Cui, Laras Fadillah, Tianhong Huang, Zetao Xiong, Chunmei Tang, Damian Kowalski, Sho Kitano, Chunyu Zhu, Daniel R. King, Takayuki Kurokawa, Yoshitaka Aoki, Hiroki Habazaki, High strength hydrogels enable dendrite-free Zn metal anodes and high-capacity Zn-MnO_2 batteries via a modified mechanical suppression effect, *J. Mater. Chem. A* **10**, 3122-3133 (2022).
63. Zhiyang Zheng, Xiongwei Zhong, Qi Zhang, Mengtian Zhang, Lixin Dai, Xiao Xiao, Jiahe Xu, Miaolun Jiao, Boran Wang, Hong Li, Yeyang Jia, Rui Mao, Guangmin Zhou, An extended substrate screening strategy enabling a low lattice mismatch for highly reversible zinc anodes, *Nat. Commun.* **15**, 753 (2024).

ARTICLE IN PRESS

64. Miaolun Jiao, Lixin Dai, Hong-Rui Ren, Mengtian Zhang, Xiao Xiao, Boran Wang, Jinlong Yang, Bilu Liu, Guangmin Zhou, Hui-Ming Cheng, A polarized gel electrolyte for wide-temperature flexible zinc-air batteries, *Angew. Chem. Int. Ed.* **62**, e202301114 (2023).
65. Zhexuan Liu, Jiachang Liu, Xiao Xiao, Zhiyang Zheng, Xiongwei Zhong, Qingjin Fu, Shaogang Wang, Guangmin Zhou, Unraveling paradoxical effects of large current density on Zn deposition, *Adv. Mater.* **36**, 2404140 (2024).
66. Junnan Hao, Libei Yuan, Yilong Zhu, Xiaowan Bai, Chao Ye, Yan Jiao, Shizhang Qiao, Low-cost and non-flammable eutectic electrolytes for advanced Zn-I_2 batteries, *Angew. Chem. Int. Ed.* **62**, e202310284 (2023).
67. Miao Sun, Guochen Ji, Meizhi Li, Junping Zheng, A robust hydrogel electrolyte with ultrahigh ion transference number derived from zincophilic "chain-gear" network structure for dendrite-free aqueous zinc ion battery, *Adv. Funct. Mater.* **34**, 2402004 (2024).
68. Kaiping Zhu, Jie Luo, Dehe Zhang, Nanyang Wang, Shibo Pan, Shujin Zhou, Zhenjie Zhang, Gengde Guo, Peng Yang, Yuan Fan, Shisheng Hou, Zhipeng Shao, Shizhuo Liu, Lin Lin, Pan Xue, Guo Hong, Yurong Yang, Yagang Yao, Molecular engineering enables hydrogel electrolyte with ionic hopping migration and self-healability toward dendrite-free zinc-metal anodes, *Adv. Mater.* **36**, 2311082 (2024).
69. Qing Li, Hu Hong, Jiaxiong Zhu, Zhuoxi Wu, Chuan Li, Donghong Wang, Pei Li, Yuwei Zhao, Yue Hou, Guojin Liang, Funian Mo, Huilin Cui, Chunyi Zhi, Crystal orientation engineering of perfectly matched heterogeneous textured ZnSe for an enhanced interfacial kinetic Zn anode, *ACS Nano* **17**, 23805-23813 (2023).
70. Guojin Liang, Jiaxiong Zhu, Boxun Yan, Qing Li, Ao Chen, Ze Chen, Xiaoqi Wang, Bo Xiong, Jun Fan, Jin Xu, Chunyi Zhi, Gradient fluorinated alloy to enable highly reversible Zn-metal anode chemistry, *Energy Environ. Sci.* **15**, 1086-1096 (2022).
71. Baohui Ren, Sanlue Hu, Ao Chen, Xiangyong Zhang, Hua Wei, Jingjing Jiang, Guangming Chen, Chunyi Zhi, Hongfei Li, Zhuoxin Liu, Inhibiting dendrite formation and electrode

ARTICLE IN PRESS

ARTICLE IN PRESS

corrosion via a scalable self-assembled mercaptan layer for stable aqueous zinc batteries, *Adv. Energy Mater.* **14**, 2302970 (2024).

72. Yu Wang, Bochun Liang, Jiaxiong Zhu, Geng Li, Qing Li, Ruquan Ye, Jun Fan, Chunyi Zhi, Manipulating electric double layer adsorption for stable solid-electrolyte interphase in 2.3 Ah Zn-pouch cells, *Angew. Chem. Int. Ed.* **62**, e202302583 (2023).
73. Nan Hu, Wensong Lv, Wenjian Chen, Huan Tang, Xiaoyan Zhang, Hongyu Qin, Dan Huang, Jinliang Zhu, Zhengjun Chen, Jing Xu, Huibing He, A double-charged organic molecule additive to customize electric double layer for super-stable and deep-rechargeable Zn metal pouch batteries, *Adv. Funct. Mater.* **34**, 2311773 (2024).
74. Yu Wang, Tairan Wang, Shuyu Bu, Jiaxiong Zhu, Yanbo Wang, Rong Zhang, Hu Hong, Wenjun Zhang, Jun Fan, Chunyi Zhi, Sulfolane-containing aqueous electrolyte solutions for producing efficient ampere-hour-level zinc metal battery pouch cells, *Nat. Commun.* **14**, 1828 (2023).
75. Guojin Liang, Zijie Tang, Bing Han, Jiaxiong Zhu, Ao Chen, Qing Li, Ze Chen, Zhaodong Huang, Xinliang Li, Qi Yang, Chunyi Zhi, Regulating inorganic and organic components to build amorphous-ZnF_x enriched solid-electrolyte interphase for highly reversible Zn metal chemistry, *Adv. Mater.* **35**, 2210051 (2023).
76. Kaiyue Zhu, Xiling Niu, Weili Xie, Hanmiao Yang, Weikang Jiang, Manxia Ma, Weishen Yang, An integrated Janus hydrogel with different hydrophilicities and gradient pore structures for high-performance zinc-ion batteries, *Energy Environ. Sci.* **17**, 4126-4136 (2024).

ACKNOWLEDGEMENTS

The authors are grateful to the funding supported from the National Natural Science Foundation of China (U25A20628, 22561160129, 22479074, 22475096 from Z.J. and 22425106, 22271139 from C.H.L.), the Equipment Pre-Research and Ministry of Education Joint Fund (8091B02052407, Z.J.), the Fundamental Research Program Key Project of Jiangsu Province (BK20253008, Z.J.), the Natural Science Foundation of Jiangsu Province (BK20240400,

ARTICLE IN PRESS

BK20241236, Z.J.), the Science and Technology Major Project of Jiangsu Province (BG2024013, Z.J.), the Scientific and Technological Achievements Transformation Special Fund of Jiangsu Province (BA2023037, Z.J.), the Academic Degree and Postgraduate Education Reforming Project of Jiangsu Province (JGKT24_C001, Z.J.), the Key Core Technology Open Competition Project of Suzhou City (SYG2024122, Z.J.), the Open Research Fund of Suzhou Laboratory (SZLAB-1308-2024-TS005, Z.J.), the Chenzhou National Sustainable Development Agenda Innovation Demonstration Zone Provincial Special Project (2023sfq11, Z.J.), and the Fundamental Research Funds for the Central Universities (020514380294, C.H.L.).

AUTHOR CONTRIBUTIONS

Z.J. conceived the idea of this study. T.Y.S. and Z.J.C. designed the experiments. T.Y.S., Z.J.C., J.Y.W., K.X.H., W.M., J.C.L., and H.G.L. performed sample preparations. T.Y.S., Z.J.C., Y.M.Y., and Z.X.T. performed electrochemical measurements, battery tests, and data analyses. T.Y.S., and Y.X.Y. performed the theoretical calculations. Z.J., C.H.L., T.Y.S., Z.J.C., and Q.C.Y. wrote the manuscript. Z.J. and C.H.L. supervised the project. All authors participated in the scientific discussion of this project.

ARTICLE IN PRESS

COMPETING INTERESTS

The authors declare no competing interests.

FIGURE LEGENDS

Fig. 1 Design, preparation, and characterizations. a, The flowcharts for preparing deep-eutectic-HE through a solvent-exchange process. **b-c**, (**b**) ATR-FTIR and (**c**) Raman spectra of deep-eutectic-HE, deep-eutectic-LE, non-eutectic-HE, non-eutectic-LE, UR, and $Zn(ClO_4)_2$, respectively. **d-g**, (**d**) SEM image, (**e**) AFM image, (**f**) XRD patterns, and (**g**) SAXS patterns of deep-eutectic-HE. The inset in (**g**) is 2D SAXS patterns of deep-eutectic-HE. Source data for (**b, c, f, g**) are provided as a Source Data file.

ARTICLE IN PRESS

Fig. 2 Mechanical properties and temperature tolerance. a-b, (**a**) Tensile-strain curves, (**b**) elastic modulus, and toughness of deep-eutectic-HE and non-eutectic-HE. The error bars in (**b**) indicate the standard deviation (SD). **c-d**, Photographs of deep-eutectic-HE (with a thickness of 6 μm) lifting heavy objects. **e-f**, DSC curves of various electrolytes in (**e**) low and (**f**) high temperature ranges. **g**, Temperature dependence of G′ and G″ for deep-eutectic-HE and non-eutectic-HE. **h-i**, (**h**) MD simulation snapshot and (**i**) corresponding Zn^{2+} solvation structure of deep-eutectic-HE. **j-l**, (**j**) Number of hydrogen bonds between H_2O molecules, (**k**) RDF, coordination number and (**l**) Zn^{2+} diffusion coefficient in various electrolytes calculated via MD simulation. Source data for (**a, b, e, f, g, j, k, l**) are provided as a Source Data file. Source data for (**h-i**) are provided as Supplementary Data 1-2.

Fig. 3 Electrochemical performances. a-c, (**a**) Ionic conductivities, (**b**) Zn^{2+} transference numbers, and (**c**) interfacial impedances of deep-eutectic-HE, deep-eutectic-LE, non-eutectic-HE, and non-eutectic-LE at different temperatures, respectively. The error bars in (**a-b**) indicate SD. Points, lines and the inset in (**c**) are experimental data, fitting results and equivalent circuit, respectively. R_0, R_{el}, and CPE in equivalent circuit are body resistance, interface impedance of electrode/electrolyte, and constant phase element, respectively, with corresponding values detailed in Supplementary Table 5. **d-h**, (**d**) Rate performances, (**e**) Tafel curves, and (**f-h**) galvanostatic cycling stabilities of Zn||Zn symmetric batteries at various temperatures of (**f**) 20 °C, (**g**) −40 °C, and (**h**) 80 °C, respectively. **i**, Performance comparisons between the deep-eutectic-HE and other recently reported HEs in terms of fracture strength, ionic conductivity, electrochemical stability window, and low-/high-temperature tolerance. The source of the literature data shown in (**i**) can be found in Supplementary Table 6-7. Source data for (**a-i**) are provided as a Source Data file.

Fig. 4 Zinc electro-plating/stripping behaviors. a-b, (**a**) Potential-time curves and (**b**) their enlarged views of Zn||Cu half batteries assembled with deep-eutectic-HE and deep-eutectic-LE,

ARTICLE IN PRESS

respectively. **c-d**, (**c**) Voltage profiles during the initial Zn deposition process and (**d**) CV curves of Zn||Cu half batteries assembled with deep-eutectic-HE and deep-eutectic-LE, respectively. **e-g**, (**e**) XRD patterns and (**f-g**) SEM images of Zn electrodes retrieved from Zn||Zn symmetric batteries assembled with (**f**) deep-eutectic-HE and (**g**) non-eutectic-LE after Zn electro-plating/stripping processes. Source data for (**a-e**) are provided as a Source Data file.

Fig. 5 Electrochemical performances of zinc-metal batteries. a, Schematic configuration of thinner-than-paper Zn||I_2 battery based on deep-eutectic-HE. **b** Rate performances of Zn|deep-eutectic-HE|I_2 and Zn|deep-eutectic-LE|I_2 batteries at 0.5 to 10 A g^{-1} with a negative/positive (N/P) ratio of 18.50–55.50. **c-e**, Long-term cycling stability of Zn||I_2 batteries at the current density of 5 A g^{-1} with a negative/positive (N/P) ratio of 18.50–55.50 at various temperature of (**c**) 20 °C, (**d**) −40 °C, and (**e**) 80 °C. **f**, Comparisons between Zn|deep-eutectic-HE|I_2, Zn|deep-eutectic-HE|V_2O_5, and other recent reported zinc-metal batteries in terms of specific energy and volumetric energy density (calculated based on the entire soft-packaged pouch battery assembly: discharge energy divided by the total mass or total volume encompassing the polyimide encapsulation material, positive electrode, deep-eutectic hydrogel electrolyte, and negative electrode). The source of the literature data shown in (**f**) can be found in Supplementary Table 8. Source data for (**b-f**) are provided as a Source Data file.

ARTICLE IN PRESS

ARTICLE IN PRESS

Editor's Summary

Flexible batteries often fail under harsh conditions. Here, authors developed a hydrogel electrolyte via synergism of nanophase separation, hydrated eutectic solvation, and hydrogen-bond networks, enabling flexible Zn||I_2 batteries with high specific energy and long lifespan across −40 to 80 °C.

Peer Review Information: *Nature Communications* thanks Junnan Hao and the other, anonymous, reviewer(s) for their contribution to the peer review of this work. A peer review file is available.

ARTICLE IN PRESS

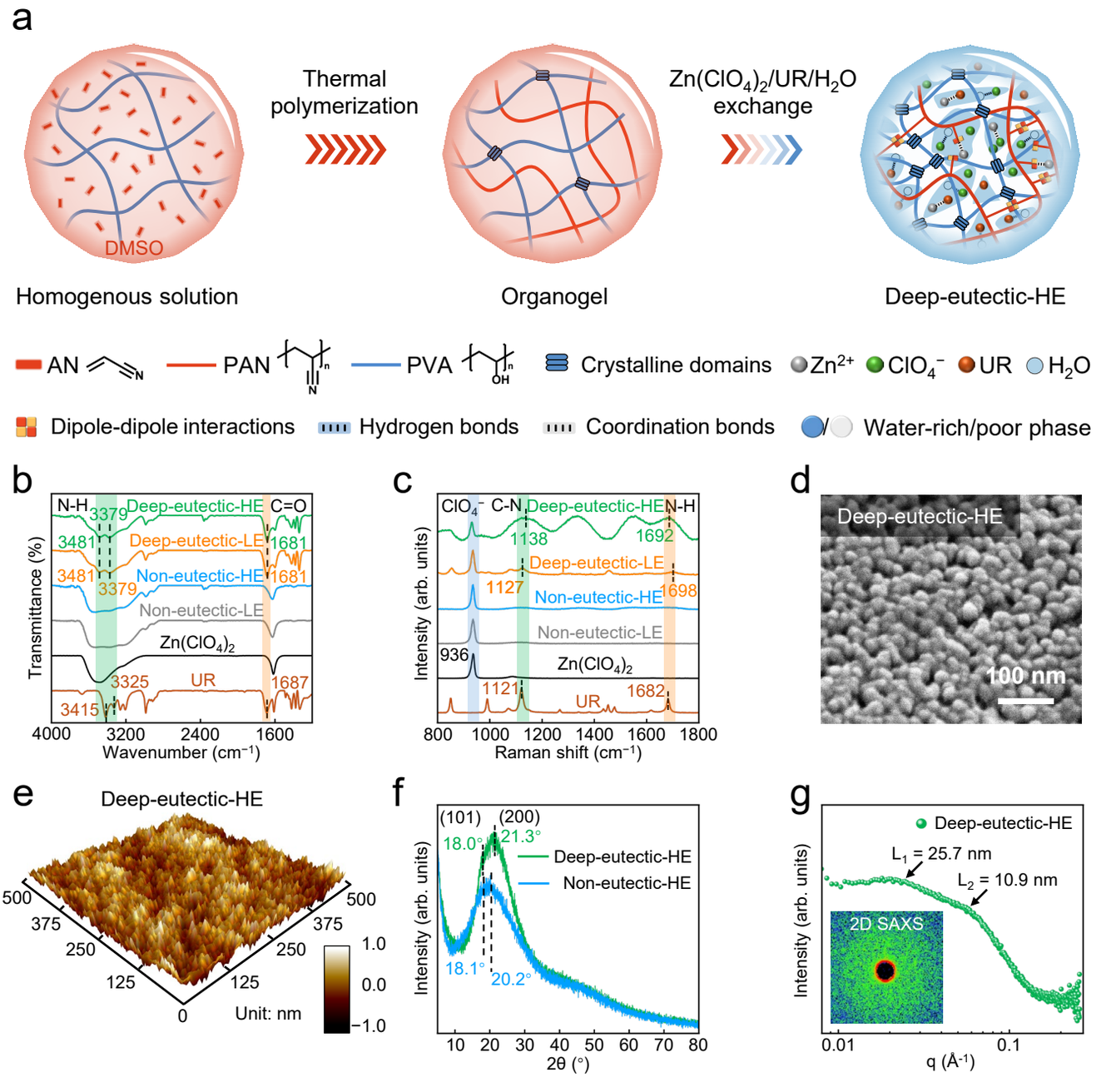
a
DMSO
Thermal polymerization
Zn(ClO4)2/UR/H2O exchange
Homogenous solution
Organogel
Deep-eutectic-HE
AN
PAN
PVA
Crystalline domains
Zn2+
ClO4−
UR
H2O
Dipole-dipole interactions
Hydrogen bonds
Coordination bonds
Water-rich/poor phase
b
N-H
C=O
Deep-eutectic-HE
Deep-eutectic-LE
Non-eutectic-HE
Non-eutectic-LE
Zn(ClO4)2
UR
3379
3481
1681
3325
3415
1687
Transmittance (%)
Wavenumber (cm−1)
c
ClO4− C-N
N-H
1138
1692
1127
1698
936
1121
1682
Intensity (arb. units)
Raman shift (cm−1)
d
Deep-eutectic-HE
100 nm
e
Deep-eutectic-HE
Unit: nm
f
(101)
(200)
18.0°
21.3°
18.1°
20.2°
Deep-eutectic-HE
Non-eutectic-HE
Intensity (arb. units)
2θ (°)
g
Deep-eutectic-HE
L1 = 25.7 nm
L2 = 10.9 nm
2D SAXS
Intensity (arb. units)
q (Å-1)

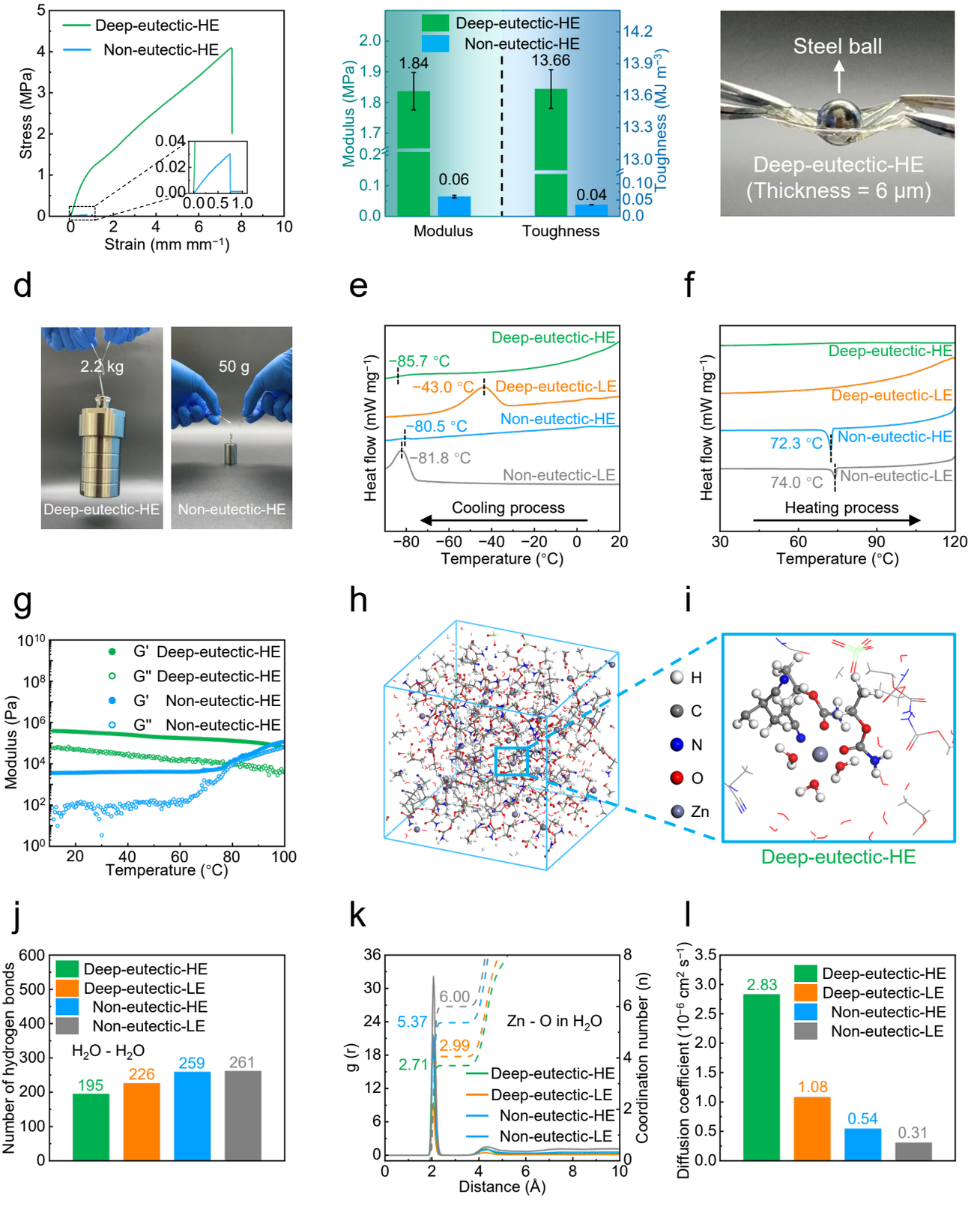
a
Deep-eutectic-HE
Non-eutectic-HE
Stress (MPa)
Strain (mm mm⁻¹)
b
Deep-eutectic-HE
Non-eutectic-HE
1.84
0.06
13.66
0.04
Modulus (MPa)
Toughness (MJ m⁻³)
Modulus
Toughness
c
Steel ball
Deep-eutectic-HE
(Thickness = 6 μm)
d
2.2 kg
50 g
Deep-eutectic-HE
Non-eutectic-HE
e
Deep-eutectic-HE
−85.7 °C
−43.0 °C
Deep-eutectic-LE
Non-eutectic-HE
−80.5 °C
−81.8 °C
Non-eutectic-LE
Heat flow (mW mg⁻¹)
Cooling process
Temperature (°C)
f
Deep-eutectic-HE
Deep-eutectic-LE
72.3 °C
Non-eutectic-HE
74.0 °C
Non-eutectic-LE
Heat flow (mW mg⁻¹)
Heating process
Temperature (°C)
g
G' Deep-eutectic-HE
G'' Deep-eutectic-HE
G' Non-eutectic-HE
G'' Non-eutectic-HE
Modulus (Pa)
Temperature (°C)
h
i
H
C
N
O
Zn
Deep-eutectic-HE
j
Deep-eutectic-HE
Deep-eutectic-LE
Non-eutectic-HE
Non-eutectic-LE
H2O - H2O
195
226
259
261
Number of hydrogen bonds
k
6.00
5.37
2.99
2.71
Zn - O in H2O
Deep-eutectic-HE
Deep-eutectic-LE
Non-eutectic-HE
Non-eutectic-LE
g (r)
Coordination number (n)
Distance (Å)
l
2.83
1.08
0.54
0.31
Deep-eutectic-HE
Deep-eutectic-LE
Non-eutectic-HE
Non-eutectic-LE
Diffusion coefficient (10⁻⁶ cm² s⁻¹)

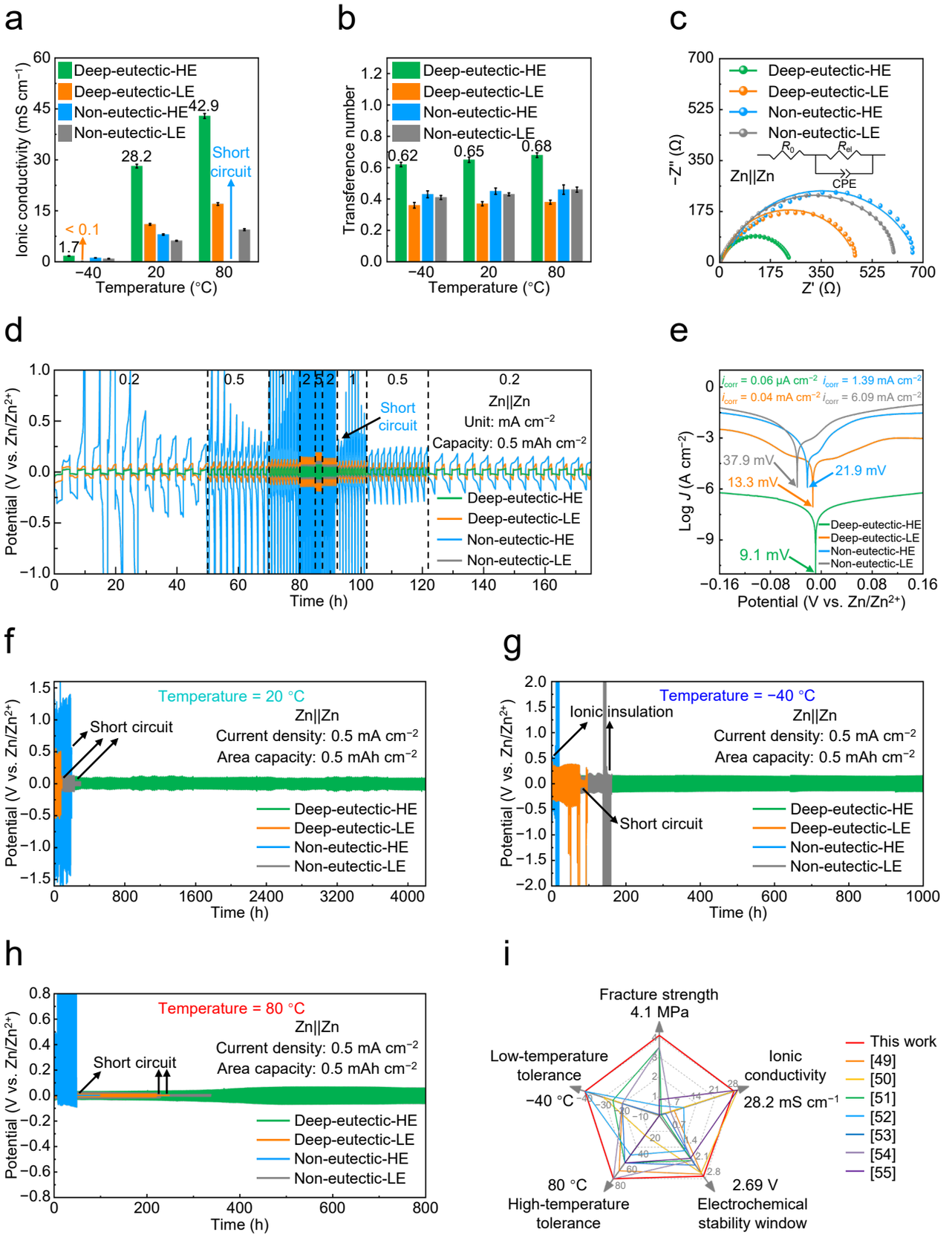
a
Ionic conductivity (mS cm⁻¹)
Deep-eutectic-HE
Deep-eutectic-LE
Non-eutectic-HE
Non-eutectic-LE
< 0.1
1.7
28.2
42.9
Short circuit
Temperature (°C)
b
Transference number
0.62
0.65
0.68
Temperature (°C)
c
−Z'' (Ω)
Z' (Ω)
Zn||Zn
CPE
d
Potential (V vs. Zn/Zn²⁺)
Time (h)
Short circuit
Zn||Zn
Unit: mA cm⁻²
Capacity: 0.5 mAh cm⁻²
e
Log J (A cm⁻²)
Potential (V vs. Zn/Zn²⁺)
37.9 mV
13.3 mV
21.9 mV
9.1 mV
f
Temperature = 20 °C
Zn||Zn
Current density: 0.5 mA cm⁻²
Area capacity: 0.5 mAh cm⁻²
Short circuit
g
Temperature = −40 °C
Ionic insulation
h
Temperature = 80 °C
i
Fracture strength
4.1 MPa
Low-temperature tolerance
−40 °C
Ionic conductivity
28.2 mS cm⁻¹
80 °C
High-temperature tolerance
2.69 V
Electrochemical stability window
This work
[49]
[50]
[51]
[52]
[53]
[54]
[55]

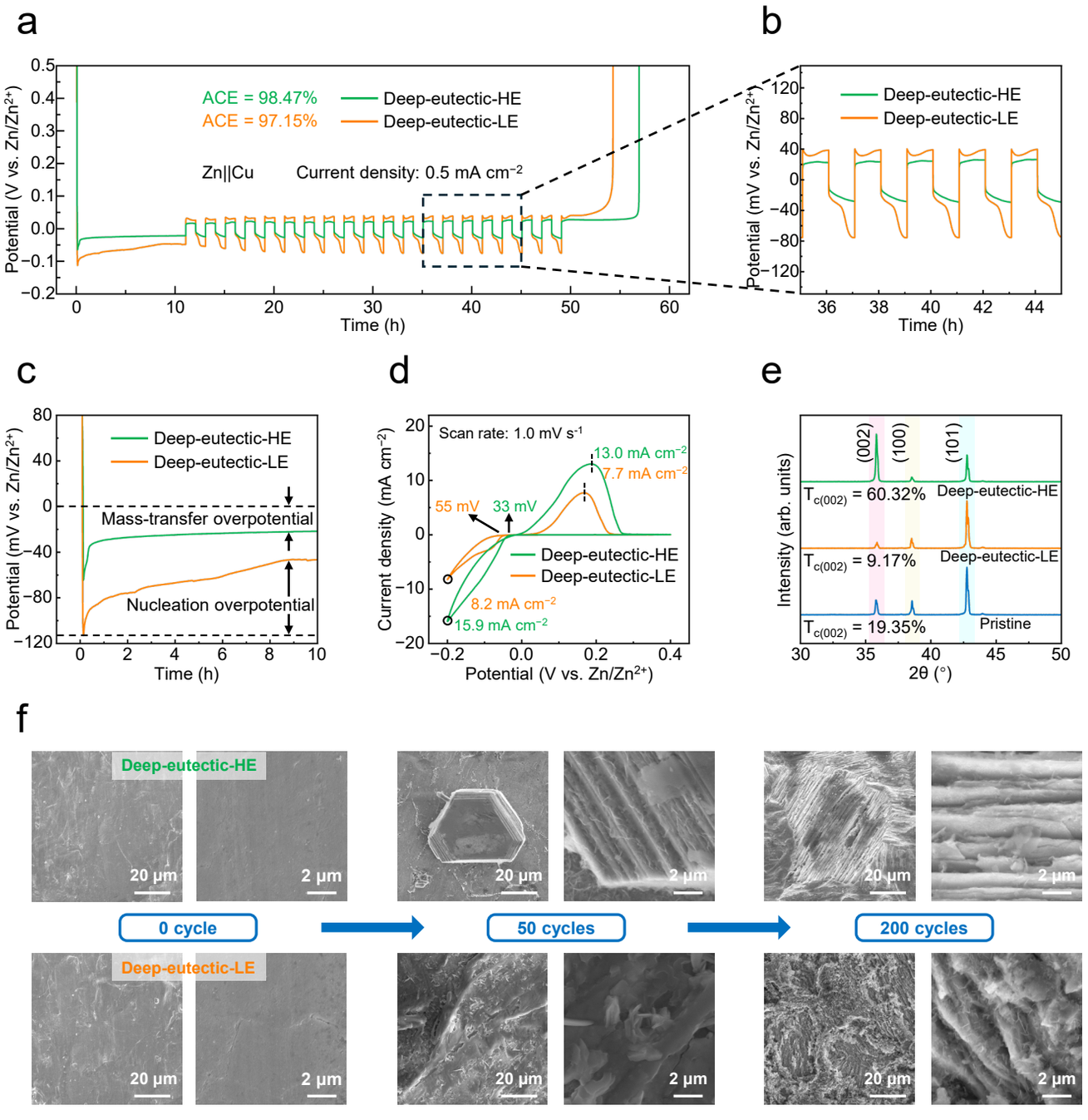
a
ACE = 98.47%
ACE = 97.15%
Deep-eutectic-HE
Deep-eutectic-LE
Zn||Cu
Current density: 0.5 mA cm−2
Potential (V vs. Zn/Zn2+)
Time (h)
b
Deep-eutectic-HE
Deep-eutectic-LE
Potential (mV vs. Zn/Zn2+)
Time (h)
c
Deep-eutectic-HE
Deep-eutectic-LE
Mass-transfer overpotential
Nucleation overpotential
Potential (mV vs. Zn/Zn2+)
Time (h)
d
Scan rate: 1.0 mV s-1
13.0 mA cm−2
7.7 mA cm−2
55 mV
33 mV
Deep-eutectic-HE
Deep-eutectic-LE
8.2 mA cm−2
15.9 mA cm−2
Current density (mA cm−2)
Potential (V vs. Zn/Zn2+)
e
(002)
(100)
(101)
Tc(002) = 60.32%
Deep-eutectic-HE
Tc(002) = 9.17%
Deep-eutectic-LE
Tc(002) = 19.35%
Pristine
Intensity (arb. units)
2θ (°)
f
Deep-eutectic-HE
20 μm
2 μm
0 cycle
50 cycles
200 cycles
Deep-eutectic-LE

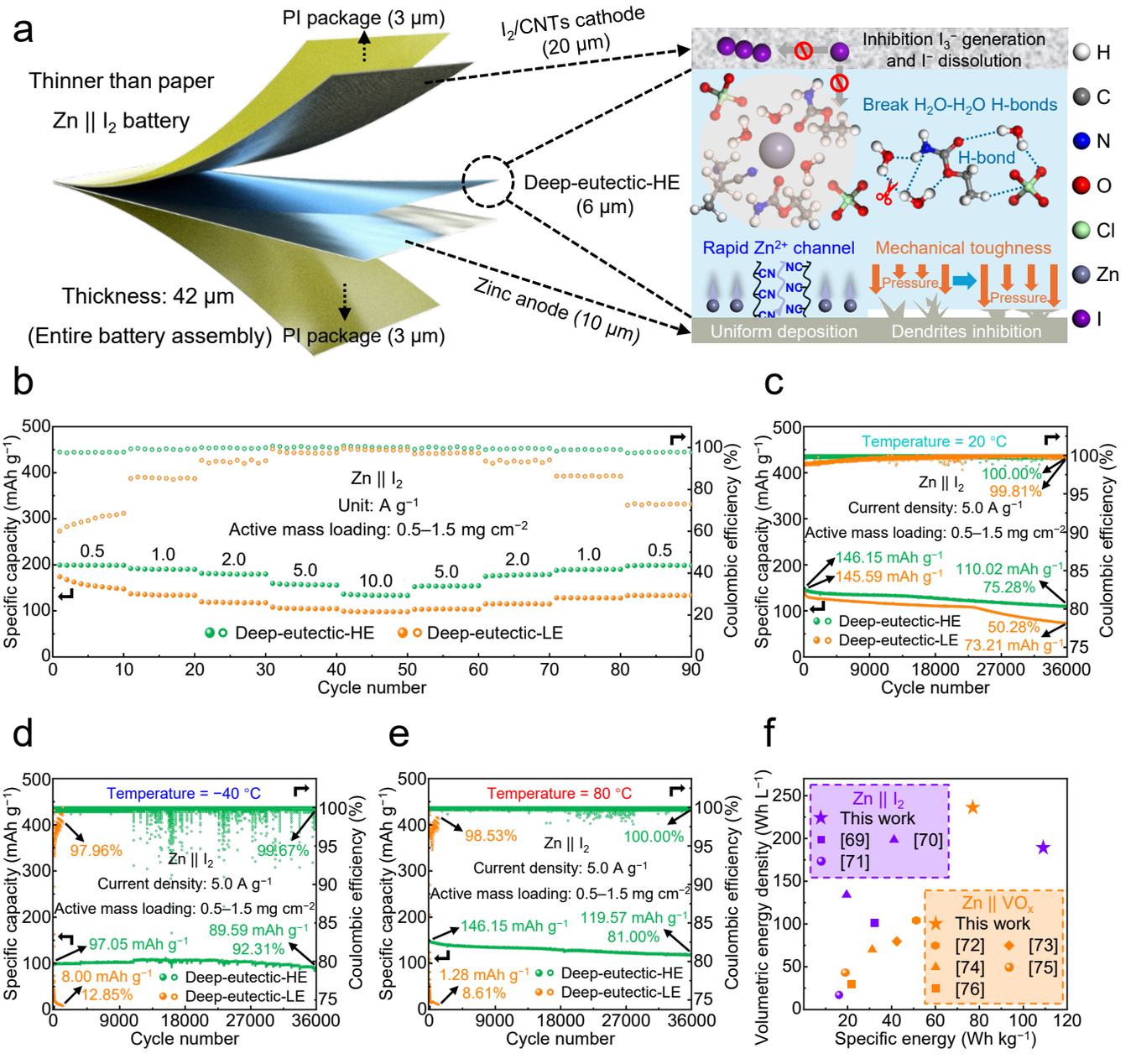
a
PI package (3 μm)
Thinner than paper
Zn || I2 battery
I2/CNTs cathode (20 μm)
Deep-eutectic-HE (6 μm)
Zinc anode (10 μm)
Thickness: 42 μm
(Entire battery assembly)
PI package (3 μm)
Inhibition I3− generation and I− dissolution
Break H2O-H2O H-bonds
H-bond
Rapid Zn2+ channel
Mechanical toughness
Pressure
Pressure
Uniform deposition
Dendrites inhibition
H
C
N
O
Cl
Zn
I
b
Zn || I2
Unit: A g−1
Active mass loading: 0.5–1.5 mg cm−2
0.5
1.0
2.0
5.0
10.0
5.0
2.0
1.0
0.5
Deep-eutectic-HE
Deep-eutectic-LE
Specific capacity (mAh g−1)
Coulombic efficiency (%)
Cycle number
c
Temperature = 20 °C
Zn || I2
100.00%
99.81%
Current density: 5.0 A g−1
Active mass loading: 0.5–1.5 mg cm−2
146.15 mAh g−1
145.59 mAh g−1
110.02 mAh g−1
75.28%
50.28%
73.21 mAh g−1
Deep-eutectic-HE
Deep-eutectic-LE
Specific capacity (mAh g−1)
Coulombic efficiency (%)
Cycle number
d
Temperature = −40 °C
97.96%
Zn || I2
99.67%
Current density: 5.0 A g−1
Active mass loading: 0.5–1.5 mg cm−2
97.05 mAh g−1
89.59 mAh g−1
92.31%
8.00 mAh g−1
12.85%
Deep-eutectic-HE
Deep-eutectic-LE
Specific capacity (mAh g−1)
Coulombic efficiency (%)
Cycle number
e
Temperature = 80 °C
98.53%
Zn || I2
100.00%
Current density: 5.0 A g−1
Active mass loading: 0.5–1.5 mg cm−2
146.15 mAh g−1
119.57 mAh g−1
81.00%
1.28 mAh g−1
8.61%
Deep-eutectic-HE
Deep-eutectic-LE
Specific capacity (mAh g−1)
Coulombic efficiency (%)
Cycle number
f
Zn || I2
This work
[69]
[70]
[71]
Zn || VOx
This work
[72]
[73]
[74]
[75]
[76]
Volumetric energy density (Wh L−1)
Specific energy (Wh kg−1)